
Effect of nanocomposite coating via EPD on bone regeneration and antibacterial properties of additively manufactured porous titanium

May 31, 2017



Effect of nanocomposite coating via EPD on bone regeneration and antibacterial properties of additively manufactured porous titanium

By

Bas Spijker

Delft University of Technology

Biomedical Engineering (BME)

Msc Biomedical Engineering

Biomaterials and Tissue Biomechanics

Daily supervisor: Dr. S. Amin Yavari

Supervisors: Prof. H. H. Weinans
Dr. A. A. Zadpoor

Content

- Abstract..... 4
- Graphical abstract..... 5
- 1. Introduction 6
 - 1.1 Background 6
 - 1.2 Implant design..... 7
 - 1.3 Surface treatments 8
 - 1.4 Hydrogel coatings 8
 - 1.5 Composite coatings..... 9
 - 1.6 Electrophoretic deposition 10
 - 1.7 Investigation of materials 11
 - 1.7.1 Chitosan 11
 - 1.7.2 Osteogenic (nano-)materials 11
 - 1.8 Conclusion..... 14
 - 1.9 Aim of this study 15
- 2. Materials & methods 16
 - 2.1 Materials 16
 - 2.1.1 Graphene oxide..... 16
 - 2.1.2 Porous titanium..... 16
 - 2.2 Particle size distribution..... 17
 - 2.3 Zeta potential..... 18
 - 2.4 Electrophoretic deposition 18
 - 2.5 Surface characterization 19
 - 2.5.1 Topography 19
 - 2.5.2 Local Surface chemical composition 19
 - 2.5.3 Thickness & degradation..... 19
 - 2.5.4 Release profile 19
 - 2.6 Cell culturing & sterilization..... 20
 - 2.7 Cell viability & Cytotoxicity 21
 - 2.7.1 Cell seeding efficiency..... 21

2.7.2 Attached cells viability & cytotoxicity	21
2.7.3 Monolayer viability & cytotoxicity	22
2.8 ALP activity	22
2.9 Osteogenic differentiation	22
2.10 Antibacterial effect	23
2.10.1 CFU	23
2.10.2 SEM	23
2.11 Statical analysis	23
3. Results	24
3.1 Particle size distribution.....	24
3.2 Zeta potential.....	25
3.3 Topology.....	25
3.3.1 Local surface chemical composition	28
3.4 Release profile	29
3.5 Pre-selection study	30
3.5.1 Si.....	30
3.5.2 HA.....	31
3.5.3 Sr	32
3.5.4 GO	33
3.6 Antibacterial effect	34
3.7 Cytotoxicity	37
3.8 ALP activity.....	39
3.9 Cell morphology.....	39
3.10 Gene expression.....	41
4. Discussion.....	42
4.1 Material characterization.....	42
4.2 In Vitro assessment.....	44
4.3 Limitations & future research	46
5. Conclusion.....	47
References	48

Abstract

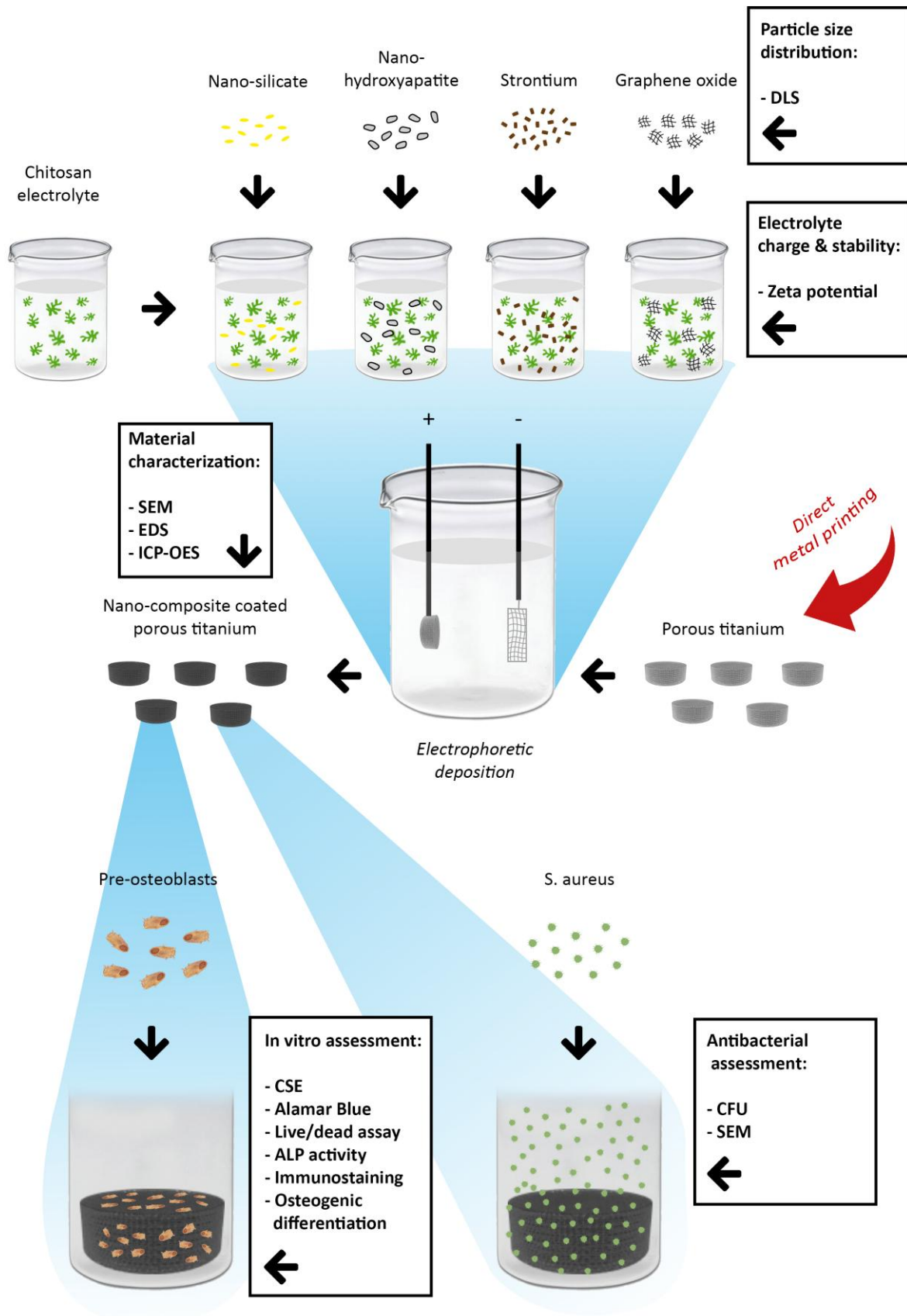
Introduction Titanium is, primarily because of its decent mechanical properties, biocompatibility, and bio-inert features, an excellent candidate for biomedical applications. The recent progress in additive manufacturing techniques provides a window of opportunity for the design of novel complex porous metal implants for bone regeneration. Current issues of bone implants: infection and aseptic loosening, could be prevented by biofunctionalization of the large surface area of porous titanium. Biomimetic, biodegradable, and biocompatible hydrogels can be co-deposited with therapeutic inorganic (nano-)materials, in the form of a (nano-)composite coating, for this dual application. The electrochemical coating process of electrophoretic deposition (EPD) can be employed to successfully deposit (nano-)composite coatings on the surface of porous metals. In this study, 3D printed porous titanium was biofunctionalized by EPD of several (nano-)composite coatings. This approach was evaluated by consecutive assessment of material characteristics, in vitro antibacterial efficiency, and in vitro cytotoxicity and osteogenic performance.

Materials & method Porous titanium scaffolds were fabricated by direct metal printing (DMP). (Nano-) composite coatings were created by co-deposition by EPD of the naturally derived hydrogel chitosan (CH) with separate inorganic (nano-)materials: nano-silicate (Si), nano-hydroxy apatite (HA), strontium (Sr), and graphene oxide (GO). Prior to EPD, particle size distribution (DLS) and stability of the electrolyte suspension (Zeta potential) was determined. Scanning electron microscopy (SEM) was conducted to evaluate the surface morphology, followed by chemical analysis by energy-dispersive X-ray spectroscopy (EDS). The release profile of the coatings was analysed by inductively coupled plasma mass spectroscopy (ICP-OES). The antibacterial efficiency was evaluated using the colony forming unit assay (CFU) and SEM with *S. Aureus* bacteria. Cytotoxicity and osteogenic performance was investigated with MC3T3 cells by evaluating cell seeding efficiency (CSE), cell viability (alamar blue & live/dead assay), ALP activity, cell morphology (immunostaining), and osteogenic differentiation (qPCR).

Results DLS verified the nano-size components of Si. Zeta potential measurements confirmed a sufficient stability required for EPD for all electrolyte suspensions. The successful deposition of all (nano-)composite coatings was validated by SEM and EDS. Moreover, the release profile study proved effective (burst) release of ions. The (nano-)composite coatings showed no significant improved antibacterial efficiency against both adherent and planktonic bacteria. CH's cytotoxic effect is mainly applicable to attached cells. Only GO showed significant higher cell viability and proliferation, compared to ASM and CH. No significant differences in ALP activity and osteogenic differentiation were observed.

Conclusion Successful deposition of (nano-)composite coatings did not result in a significant improvement of antibacterial efficiency, cytocompatibility, and osteogenic performance, when compared to both as manufactured and chitosan-coated porous titanium.

Graphical abstract



1. Introduction

1.1 Background

In the last decade, the worldwide orthopedic market has steadily grown from \$27.2 billion in 2007 to \$35.5 billion in 2013, and is forecasted to grow 3.5% annually [1]. This tendency can be explained by factors including the growing world population, the increasing welfare, the increasing number of elderly people, the popularity of active lifestyles, and the raised life expectancy [2]. Total joint replacement and reconstructive bone surgery are two of the most frequently performed orthopedic procedures [3], and although both procedures are regarded successful, the limitations incite researches to further increase their potential. The main issues of current joint replacing implants are aseptic loosening and infection [4, 5], where for bone reconstruction limited availability of ‘golden standard’ autologous bone tissue, and reduced healing potential of above critical-sized bone defects reduce the effectiveness and applicability [6, 7].

The underlying mechanisms of the limitations of these procedures can be elucidated by inspection of the biological characteristics and processes which play a role in the natural healing process of bone tissue. Bone tissue can be characterized based on its composition: approximately 60 wt% bone mineral, 15 wt% collagen, and 15 wt% water [8]; and based on its structure: bone densities and morphologies differing depending on location and scale (figure 1) [8-10]. In contrast to most other tissues, bone has

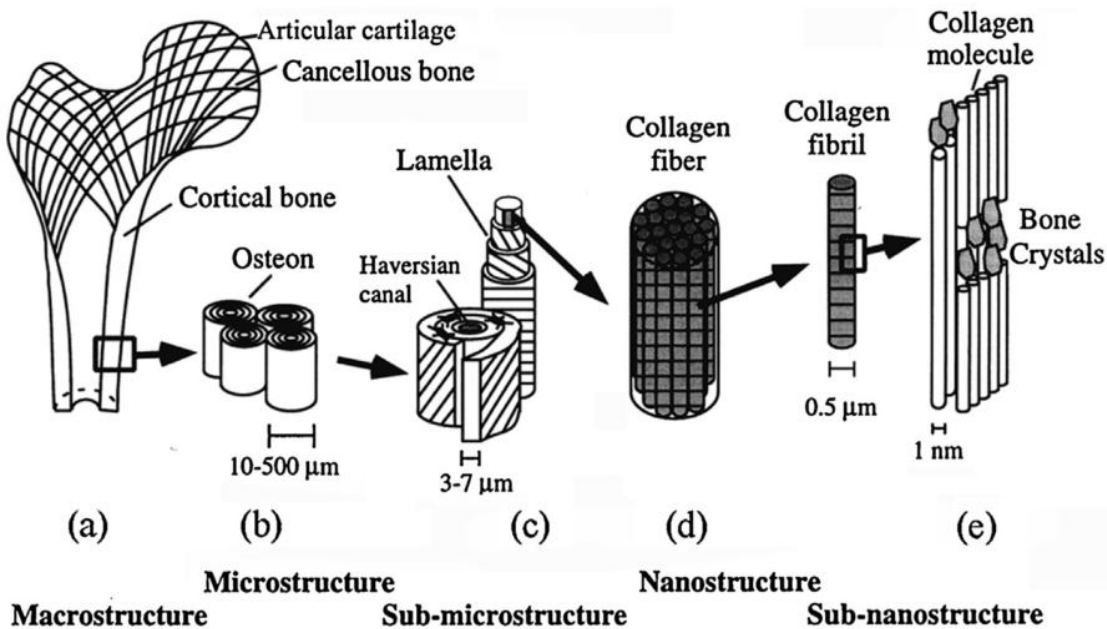


Figure 1: Structure of cortical bone [Wu et al. 2004]

the unique potential to reconstruct and remodel itself, after it has been damaged, without significant scar formation [11]. This healing process has, apart from an accurate spatiotemporal planning, a few other essential prerequisites: mobility of mesenchymal stem cells (MSCs), which orchestrate the healing process; revascularization, in order to transport the indispensable metabolic (waste) products and regulatory molecules such as growth factors; and finally, mechanical fixation and stimulation [12-15]. The necessity of mechanical stimulation originates from the bone remodeling process. This process can be described by Wolff's law: the net result of the simultaneous bone formation and resorption found in bone tissue is depending on mechanical stimulation, higher loads will lead to higher bone density and visa versa [15].

Based on these underlying mechanisms, today's limitations can be explained: aseptic implant loosening could originate from inadequate bone ingrowth or unequal load distributions along implant and surrounding bone, in which case local bone resorption, following Wolff's law, in the end leads to loosening [16]; infection risks arise from the insufficiency of the body's defense mechanism against artificially introduced bacteria during surgery [17]; Present artificial bone grafts lack the resemblance to the natural composition and structure, and pre-existing vascular network that autologous bone grafts possess [18]; And critical-sized bone defects cannot be bridged due to a lack of a sufficient (vascular) network to transport essential metabolic products, MSCs, and biomolecules [7].

1.2 Implant design

Titanium and its alloys have been used in the orthopedic field since the mid-1940s, and are still frequently used today, due to their favorable properties, such as: high specific strength, relatively low weight, decent corrosion resistance, and biocompatibility [19-21]. The mechanical properties are mainly determined by the presence and concentration of alloying elements and the existence of different crystal structure types [22]. Naturally, a self-regenerative nano-layer of titanium oxide (TiO_2) is passively formed on the surface of the titanium, the low reactivity of this TiO_2 -layer provides corrosion resistance and biocompatibility [23].

The implants main purpose is to provide mechanical stability at the implant location, especially during the regeneration and ingrowth of (new) bone tissue. Apart from the choice of material, the design options regarding porosity and topography can be of great importance to, not only provide mechanical stability, but also prevent stress shielding, increase the number of binding sites for bone, and allow cell mobility, vascularization, and fluid flow [16, 19].

In recent years, the advances in additive manufacturing methods (for metals) has created a great window of opportunity for the development of ingeniously porous structures. This greatly expanded the number of possibilities regarding the morphology, and the feasibility of porous implants [24-26]. Applications could be bio-mimetic implants resembling the natural bone structure, patient specific designs, or simply adjustment of mechanical properties by controlled addition of pores [27, 28].

The development of, especially interconnected, porous implants provides a number of advantages over solid implants [14, 29, 30]. Firstly, the mechanical connection between implant and bone can be improved, because of the increased number of binding sites, resulting from the enlarged surface area,

and the possibility of ingrowth of bone tissue[8]. Secondly, the stiffness of an implant can be lowered by adding porosity to the material. This can solve the mismatch between the stiffness of the implant and the surrounding bone, which is responsible for the nonuniform load transfer and thereby possible loosening [31, 32]. Thirdly, an interconnected porous network would allow cells to migrate across the implant, (neo)vascularization, and fluid flow, which are all essential for healthy bone tissue [7]. Lastly, the presence of empty cavities inside the scaffold also opens up the possibility to (partially) use this space and extra surface area for loading and controlled delivery of osteogenic or antibacterial agents, at the implant location [8, 33-35].

1.3 Surface treatments

Although the biological inertness of titanium (alloy) surface is a crucial characteristic in present biomedical applications, future designs, especially porous designs, could benefit from further biofunctionalization of the surface and free space [34, 36].

One group of methods are surface modifications: alteration of the bulk characteristics and topography of the material on macro-, micro- or nano-scale [37]. Examples are anodizing, patterning, and acid treatments [38]. The main idea behind the incentive to investigate small scale surface modifications is that a bio-mimetic hierarchical structure composed of micro and nano-scale components may provide a more suitable environment for (stem) cells [39]. On both, micro and nano-scale, for instance, higher porosity and surface roughness can facilitate bone formation [34, 40, 41]. Nano-scale structures like (titanium) nano-tubes also seem to enhance osteoblast functionality [39, 42, 43].

Alternatively, the implant surface could be coated or grafted with (thin) layers of other materials. Chemical vapor deposition, electrophoretic deposition, immersion, and plasma spraying are examples of methods which could achieve this [44]. A popular approach for biofunctionalization of the surface involves the extracellular matrix (ECM): the membrane that functions as the intracellular, mechanical, and biochemical framework of natural tissues [8, 45]. Bio-mimetic artificial replication of this membrane, in the form of a coating, is investigated to increase the biofunctionality of implants, by creating a 'cell-friendly' environment containing biological cues, especially for the first weeks after implantation [46].

1.4 Hydrogel coatings

The huge potential of hydrogels for this specific application lies in their propitious properties: biocompatibility, biomimetic water content, extra cellular matrix-like structure, biodegradability, the possibility of incorporation of specific agents, a big range of mechanical properties, and above all good controllability of all these properties [45, 47]. Supposedly, hydrogels coatings can achieve a beneficial environment for cells, resulting from a combination of their mechanical and biological features.

Hydrogels are insoluble 3D matrices, composed of cross-linked hydrophilic polymer chains, which attract large volumes of water [48]. There are two main classes of hydrogels: natural hydrogels, which are build of naturally derived polymers, and often are biocompatible and biodegradable; and synthetic hydrogels which lack superior biological characteristics but have higher reproducibility and controllability [49]. The amount and type of the cross-links, together with the type of hydrogel, define most of the important

chemical, biological, and mechanical properties, namely: biocompatibility, biodegradability, mechanical response, and solute transport & porosity [50].

Since the continuity of bone tissue relies on remodeling: a controlled and balanced local synthesis and destruction of structural elements; the biodegradability of the coating should be considered [47]. It would be most favorable, from this point of view, to use a coating which can provide the most optimal environment during regeneration and slowly make way for newly synthesized natural tissue by an ingeniously designed (bio)degradation behaviour. Total degradation and elimination of degradation products could also prevent possible negative long term responses, and would make surgical removal unnecessary [8, 47]. The biodegradability of hydrogels is determined by the ability of biological processes to breakdown the specific polymer structures [47, 51]. Chemical hydrolysis and enzymatic digestion are the main processes that drive degradation of the hydrogel structure inside the body. The hydrolysis process starts when the penetration of water through the polymer matrix results in breakage of some of the chemical bonds in the structure. This process will shorten long polymer chains into water soluble parts, which can be eliminated from the site by enzymatic activities [47]. Enzymatic digestion reduces the hydrolyzed parts into their smaller building blocks, which can be absorbed by the body (fluid) and transported [47]. The actual rate of degradation depends on many factors: the amount of cross-links, the diffusion coefficient of water, the hydrolysis rate, the hydrophilicity of the polymer, the solubility of the degradation product, the enzymatic sensitivity of the polymer, the surface area of the porous hydrogel, and the implant location [8].

Another key characteristic is the mobility of nutrients, metabolic (waste)products, and bio-active molecules, which is essential for healthy tissues. This means that the mobility of solutes in and through the hydrogel should be sufficient for local metabolism and bio-signaling to reach osteogenesis at the implant surface [52]. In that sense the porosity of the hydrogel is of corresponding importance as that of the implant itself: it determines the maximum size of solutes that can diffuse, the infiltration of cells, and the rate of vascularization [53].

Moreover, ECM-like coatings can function as a mechanical stabilizer for cells, they apply a certain amount of (pre-)tension to attached cells, which stabilizes them when its loaded through an external force [54]. Since mechanical stress can alter the response of individual cells, for instance by regulating parts of their differentiation, mimicking natural conditions could positively influence osteogenesis.

Finally, the coating should endure shear forces during and after implantation which could potentially destroy the hydrogel structure and thereby the functionality [55]. Mechanical properties can be enhanced by elevating self cross-linkage or incorporation of reinforcing molecules and particles into the polymer network, which increase the stability and the coherence of the polymer chains, by formation of additional cross-links [56].

1.5 Composite coatings

Previous research provides four groups of therapeutic agents, or combinations, to further increase the beneficial effects of coated implants, by synthesis of composite coatings: incorporation of various growth factors, providing elevated levels of these essential signaling and regulating bio-molecules [49,

57]; incorporation of inorganic (nano-)materials, which can influence properties like: osteogenic performance, mechanical stability, degradation behavior [58]; incorporation of different types of MSCs in the hydrogel matrix [59, 60]; and incorporation of medicine [61]. By using composite coatings these therapeutic agents can be introduced and released at the implantation site during the healing process, without any interference from the outside.

The efficiency of embedded (nano-)materials depends on direct contact with the body fluid and cells. This contact can be established when particles are located on the outer surface of the coating, by diffusion out of the hydrogel matrix, by (partial) degradation of the hydrogel carrier, or by degradation products of these (nano-)materials [62].

Diffusion, the movement of particles from a high concentrated area to a lower concentrated one, is considered to be the main mechanism providing mobility of embedded agents [63, 64]. The actual rate of diffusion depends on environmental conditions: pH, temperature, and fluid flow; structural characteristics: porosity, degree of swelling, and degradation speed; and particle characteristics: size, morphology, and bonding type [51].

The composite coating has a few advantages over direct coating of (nano-)materials: the on-site release of degradation products can be optimally controlled by modification of the hydrogel carrier. Secondly, the coating can be applied at room temperature, where pure inorganic deposits often rely on heating steps for densification, which can significantly damage the (porous) metal structure [65].

The incentive to develop nano-composite coatings can be explained by the augmented surface to volume ratio [66]. Smaller particles have relatively higher surface area than larger particles relative to their volume, because surface area scales with a lower order than volume does. A greater surface area means a greater potential to interact with body fluid and cells, which is essential to achieve osteogenic stimulation. Other features of small particles are higher mobility (diffusion) and higher uniformity of coating [8].

1.6 Electrophoretic deposition

During the last decades, various methods have been developed which can formate a hydrogel composite coating on a substrate [8, 46]. Examples are self-assembled monolayers (SAM), the layer-by-layer method (LbL), and a broad group of (electro)chemical methods [51, 67-70]. The electrophoretic deposition method (EPD) is one of the most promising methods because of its advantageous properties: versatility in terms of choice of materials, tunability of coating thickness, little restriction of the morphology of the substrate, decent controllability over coating parameters, short formation time, and simple one-step processing [71, 72].

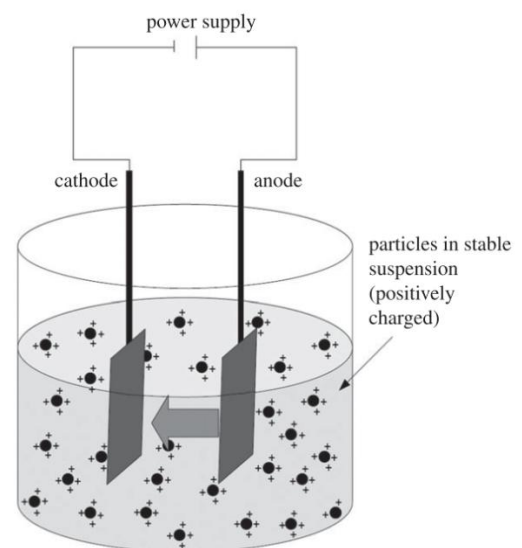


Figure 2: Electrophoretic deposition

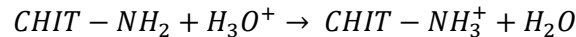
EPD uses electrophoresis, the forced movement of charged particles, in fine powder or colloidal form, under the influence of an electric field [73]. Figure 2 [65], displays a schematic overview of the typical electrophoretic deposition setup. In this case, the electric field applied through the suspension forces the positively charged particles to migrate to the negatively charged cathode and coagulate around its surface (cathodic EPD). In contrast to cathodic EPD, anodic EPD can be used to deposit negatively charged particles on the surface of the positively charged anode following the same electrophoresis mechanism [65, 72].

1.7 Investigation of materials

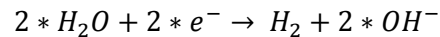
1.7.1 Chitosan

Chitosan, a natural polymer derived from the shells of crustaceans, is a promising material for biomedical applications due to its (intrinsic) favorable properties: biocompatibility, enzymatic (bio)degradability, and stimulation of tissue healing [74, 75]. In addition, chitosan can be produced at low costs and is abundant in nature. Furthermore, the positive charge of chitosan at physiological conditions provides a bactericidal potential by electrostatic interactions with the negatively charged components of the bacterial membrane [76]. Finally, chitosan can be deposited on (porous) metals by means of EPD:

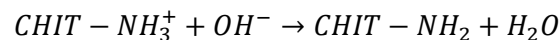
The cationic chitosan can be dissolved in water at a low pH to form a cationic poly-electrolyte[77]:



During the EPD process a high pH is generated at the surface of the cathode by the cathodic reaction of water:



This increase in pH results in a decreasing charge which leads, together with the earlier described electrophoresis of the cationic chitosan towards the cathode, to precipitation (cross-linking) of chitosan on the cathodic substrate in the form of a insoluble deposit [78, 79]:



Chitosan can be co-deposited with various (nano-)materials: by simultaneous cationic deposition with mainly positively charged (nano-)materials or ions, for instance: silicate, hydroxyapatite, strontium; or by formation of net positively charged macro molecules with negatively charged materials, graphene oxide for example, via (temporal) bonds [80].

1.7.2 Osteogenic (nano-)materials

Based on previous research, the osteogenic effects of inorganic (nano-)materials can globally be subdivided in: osteogenic stimulation by dissolution products, or by bulk properties, that directly affect the environment and surface characteristics of the coating [81]. However, the mechanisms of some effects might result from a combination of factors and cannot be fully explained yet [81]. It should be noticed that most of the reported osteogenic effects are dose-dependent and adverse effects could

arise from changes in concentration, particle size, and application [82-84]. Table 1 provides a summary of the reported osteogenic effects and mechanisms of (nano-)hydroxyapatite, (nano-)silicate, strontium (ions), and (nano-)graphene oxide.

Material	Source	Mechanism	Effect	Reference
(Nano-) Hydroxyapatite	Bulk & surface	Increased number of cell attachment sites/ protein binding sites	increased cellular attachment	[66, 85, 86]
	Dissolution product: Ca^{+}	Activation of Ca-sensitive cellular receptors	Elevated expression of osteogenic growth factors	[87]
	Dissolution product: P^{3+}	Contact with cells leads to elevated expression of matrix Gla protein	More bone formation	[88]
	Both/unclear	-	Elevated osteogenic differentiation (ALP & osteocalcin), upregulated ALP activity, mineralization, cell viability & proliferation	[66, 85, 86, 89]
(Nano-) Silicate	Bulk & surface	Increased surface roughness & increased number of protein adhesion sites	Elevated osteogenic differentiation, increased cell attachment & metabolic activity	[56, 90]
		Forms additional cross-links with hydrogel or loaded drugs	Increased coating stability & improved drug delivery	[83]
	Dissolution product: Si^{+}	Role in metabolic processes associated with bone formation & calcification	stimulate bone matrix calcification & potential to increase bone mineral density	[81, 91]
	Dissolution product: Mg^{2+}	Has a regulatory role in bone formation, cell adhesion, and osteoblast stability	Improved osteogenesis	[92, 93]
	Dissolution product: $Si(OH)^4$	Has a regulatory role in collagen 1 production and osteogenic gene expression	Up-regulated osteogenic gene expression and collagen 1	[94]

		production		
Strontium	Dissolution product: Li^+	Co-regulates the Runx-2 expression	Up-regulated Runx-2 expression	[81]
	Dissolution product: Sr^{2+}	Activation of Ca-sensitive cellular receptors & substitution for Ca in crystal structure of bone	Elevated expression of osteogenic growth factors & potential increased bone formation	[95, 96]
		Unclear/activation of Ca-sensitive cellular receptors	Increased osteoblast proliferation & ALP activity	[81, 97-101]
		Increased osteoclast apoptosis by synergistic effect with Ca	Inhibition of bone resorption	[102]
(Nano-) Graphene oxide	Bulk & surface	Possibly improved mechanical stimulation of (stem) cells by better stress distribution on the coating	Elevated OCN expression & bone deposition	[103]
		Increased number of protein adhesion sites (partially by oxygenate groups)	Improved cellular adhesion & proliferation	[104, 105]
		Unclear/mechanical properties, nano-topography & morphology	Increased ALP activity & osteogenic differentiation (both debated)	[106-108]

Table 1: Summary of osteogenic effects of selected (nano-)materials

1.8 Conclusion

There are many novel approaches to biofunctionalize orthopedic implants, the combination of porous titanium with biodegradable hydrogel coatings incorporated with osteogenic (nano-)materials is one of the promising concepts (fig. 3). Porous titanium, which provides the mechanical stability of the implant, prevents stress shielding, and allows bone ingrowth and vascularization; has a significantly enlarged surface area when compared to solid designs. This extra surface can be functionalized by a hydrogel coating, improving the environment for cellular activity, and functioning as an on-site controllable release platform for osteogenic (nano-)materials. Osteogenic (nano-)materials can further stimulate the formation of new bone tissue by improving cell activity by local alteration of the surface characteristics and release of ions.

Electrophoretic deposition (EPD), a one-step electrochemical coating process, characterized by versatility and controllability, can be employed to co-deposit hydrogels and (nano-)materials on porous metal implants.

The potential of (nano-)composite coatings on porous titanium by EPD lies in the great number of design options for the three main components: porous structure, hydrogel carrier, and (nano-)materials. By carefully tuning the components of this concept, an important transition towards patient-specific orthopedic implants could be accomplished, since bone properties, and thereby implant requirements, vary with age, location, heredity, and lifestyle [109, 110].

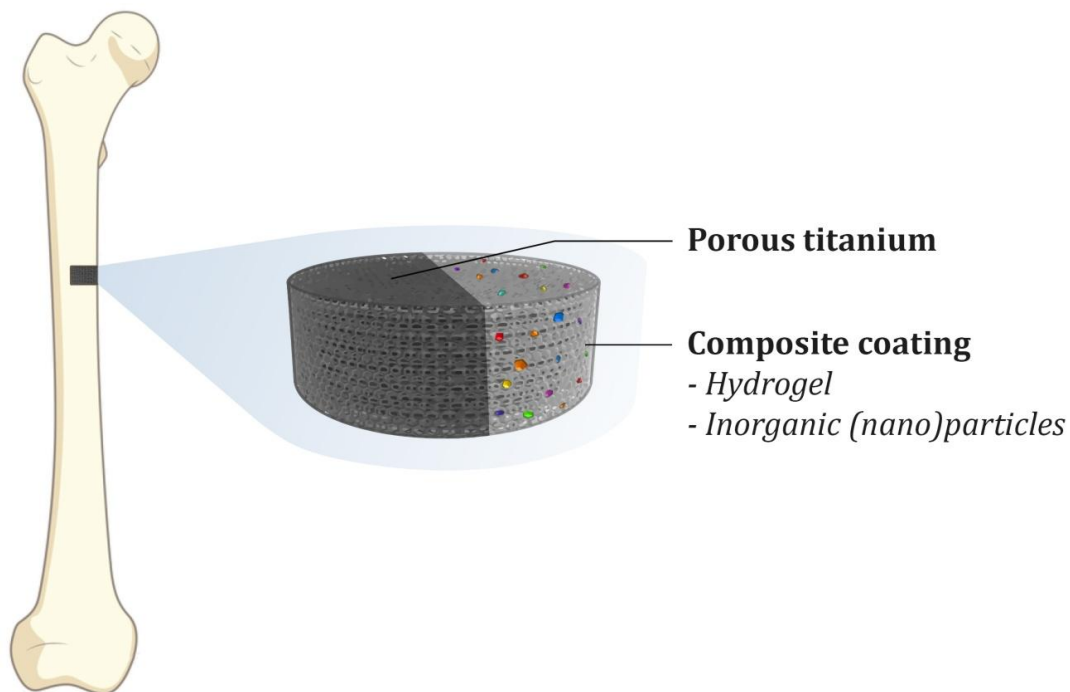


Figure 3: Composite coated porous titanium

1.9 Aim of this study

The aim of this study is to contribute to the expansion of knowledge in two specific areas: production and performance of coated porous titanium, and the in vitro effect of (nano-)composite coatings consisting of natural polymers and inorganic (nano-)materials on both osteogenesis and antibacterial performance. Although efforts have been made to investigate porous metallic implants, many aspects have not been optimized. The same is true for previously mentioned composite coatings: the components have been investigated separately on osteogenic and antibacterial effect, but most biological mechanisms, synergistic effects, and optimal designs, are not clarified at this moment. Nano-silicate, strontium, graphene oxide, and to a lesser extent nano-hydroxyapatite, have not been extensively investigated in combination with chitosan, let alone on porous titanium by EPD.

Previous research of our group confirmed chitosan's antibacterial potential and intrinsic cytotoxic features. Furthermore, it showed the successful electrophoretic deposition of a nano-composite coating for improved antibacterial efficiency.

The main question of this research project is: Could the co-deposition of aforementioned materials together with chitosan, in the form of a composite coating on porous titanium, improve chitosan's cytocompatibility and osteogenic performance, and at the same time conserve its intrinsic antibacterial potential? In order to assess the potential of the novel composite coatings the following goals are formulated:

- Successful deposition of a chitosan-(nano-)material composite coating on porous titanium by means of electrophoretic deposition
- Comprehensive material characterization, including chemical composition and release profile
- Verification of the in vitro antibacterial performance of (composite coated) porous titanium
- Extensive assessment of the in vitro cytotoxicity of (composite coated) porous titanium
- In vitro evaluation of the osteogenic performance of (composite coated) porous titanium

2. Materials & methods

2.1 Materials

Chitosan (degree of deacetylation 80%, viscosity 200-400 mPa.s) was acquired from Fluka BioChemica. Hydroxyapatite nano-powder (particle size <200nm), and strontium chloride powder were acquired from Sigma-Aldrich. Silicate (Laponite) nano-powder was acquired from BYK.

2.1.1 Graphene oxide

Graphene oxide was acquired via a research group at the TU Delft (B. Lehner). A modified Hummer and Offeman method [111, 112] was used to chemically synthesize GO. In brief, 0,5 g graphite (Pure graphite flakes NGS Trading & Consulting GmbH with an average flake size of 45 μm (Ma -399,5 RG)) was mixed on an ice bath under continuous stirring with 20 mL H_2SO_4 and 5 mL HNO_3 . The mixture was stirred for 30 min, then 3 g KMnO_4 were added (still on an ice bath). The mixture was stirred again for 30 minutes and incubated on the ice bath for one hour. The sample was heated to 35°C for 3 hours and diluted with 40 mL ultrapure water. The mixture was incubated at 35°C for 2 hours, and then 100 mL ultrapure water was added. Finally, 3 mL H_2O_2 (30%) was slowly added, and the mixture was washed, centrifuged (1500rpm), and sonicated (2h).

2.1.2 Porous titanium

Porous titanium scaffolds were manufactured by direct metal printing (DMP), using a ProX DMP 320 (Layerwise NV, Belgium). Spherical (pure) titanium powder (ASTM 67) was used as input material. The selective laser melting process was conducted in an inert gas atmosphere (oxygen concentration lower than 50 ppm). Scaffolds were removed from the titanium substrate using wire electrical discharge machining (EDM). All scaffolds were completely cleaned in three steps (10% acetone, 70% ethanol, ultrapure water) using sonification (ultra sonic bath) before continuing with coating and analysing. Figure 4 displays the morphology of the additively manufactured porous titanium scaffolds.

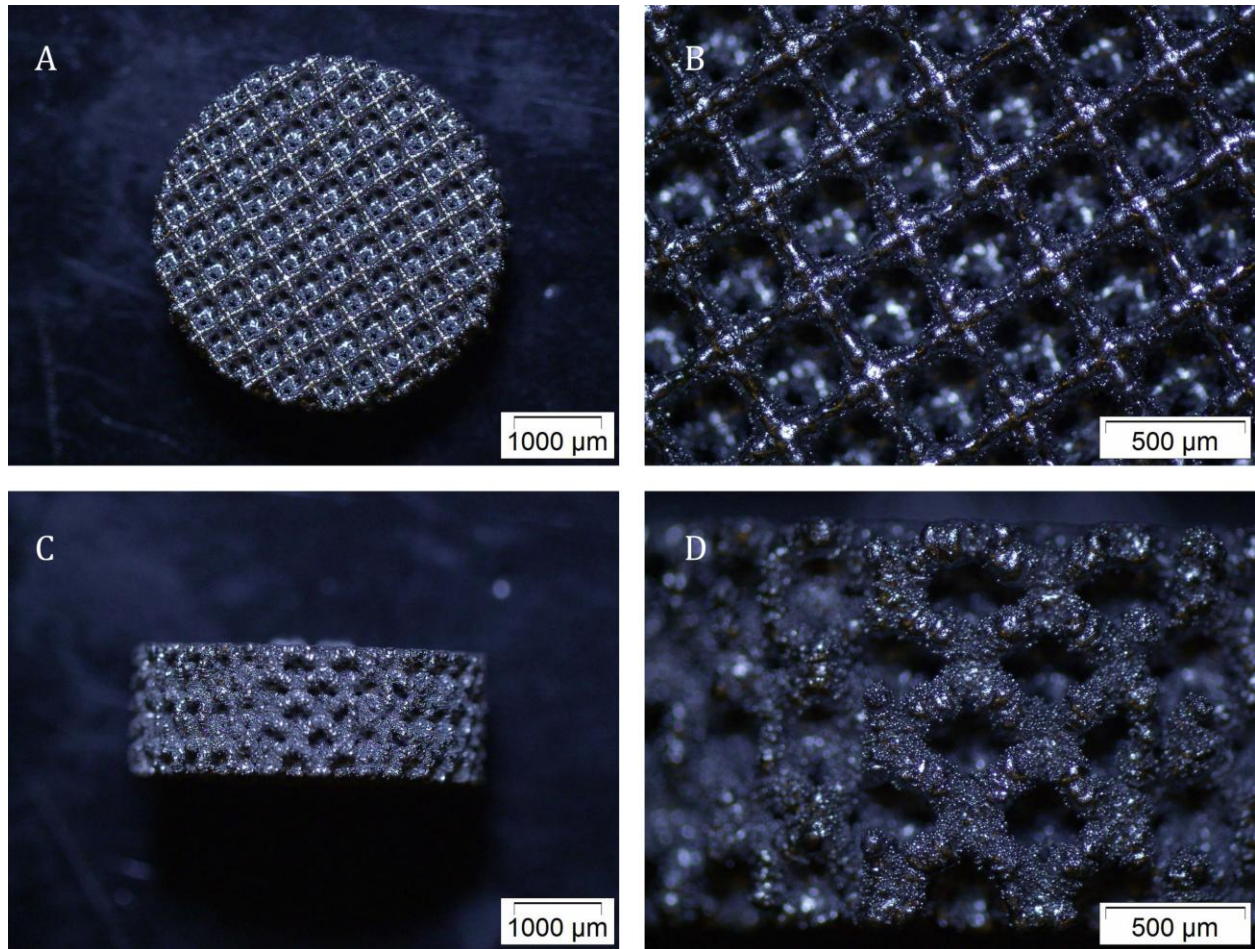


Figure 4: Additive manufactured porous titanium scaffold (A,B) top view (C,D) side view

The dimensions, relative density, and average strut density (OHAUS Pioneer PA214C balance) of the scaffolds can be found in tabel 2. The scaffold morphology is composed of dodecahedron unit cells, which were designed using the Magics program (Materialise, Leuven, Belgium).

Characteristic	Specification
Diameter	8.13 ± 0.02 mm
Height	3.15 ± 0.03 mm
Relative density	37.19 ± 0.83 %
Average strut density	98.78 ± 0.63 %

Table 2: characteristics titanium scaffold

2.2 Particle size distribution

The particle size distribution of the acquired hydroxyapatite nano-powder, strontium chloride powder, silicate (Laponite) nano-powder, and graphene oxide dissolved in water was accessed using the direct laser scattering (DLS) method (Malvern ALV CGS-3). Small amounts of each material were dissolved in 1ml of miliQ water and dispersed by sonification (15 min) (in ultra-sonic bath) prior to the

measurements. The DLS measurements were conducted at room temperature (25 degrees Celsius). During DLS, a laser was pointed through the dispersion while time-dependent fluctuations in the photon count rate, induced by the light scattering of the dispersed particles in the sample, were measured (under an angle of 90 degrees). First the material concentration of each material was optimized to reduce the amount of distortion caused by re-scattering of the scattered light by other particles. The optimal concentration was reached by diluting or concentrating the samples until the right range of registered scattering events was reached. After optimization, the detected fluctuations of the photon count rate could be directly related to the hydrodynamic diameter, the diameter of the particle plus a hydration layer, and the related size distribution.

2.3 Zeta potential

The stability, absolute charge value, and polarity, of the electrolyte suspensions were evaluated prior to the electrophoretic deposition process by zeta potential measurements for all experimental groups (Zetasizer Nano-Z). Zeta potential measurements were conducted at room temperature (n=3), resembling the conditions during EPD.

2.4 Electrophoretic deposition

The electrolyte suspension was created by dissolving chitosan (0.5 mg/ml) in a 1% (volume) acetic acid solution followed by approximately 15 hours of continuously stirring. The titanium scaffold functioned as the positively charged cathode, where a platinum mesh functioned as the negatively charged anode. The deposition process, during which the electrolyte suspension was moderately stirred, was characterized by a deposition time of 5 min, a DC voltage of 10 V, and was executed under controlled conditions under a fume hood. Each sample was coated using 25ml of a fresh electrolyte suspension. Afterwards, each sample was quickly rinsed in demineralized water and dried for approximately 15 hours at room temperature.

The scaffolds of the chitosan group were created by EPD using the electrolyte suspension consisting of 0.5 g/l chitosan. In contrast to the chitosan electrolyte suspensions, the other (composite) electrolyte suspensions were created by the addition of different concentrations of hydroxyapatite nano-powder (nHA), strontium chloride powder (SrCl), silicate nano-powder (nSi), or graphene oxide (GO), to the pure chitosan electrolyte suspension. Table 3 provides an overview of the composition of each electrolyte. Three concentrations for each type of the aforementioned (nano-)materials were selected based on related research [79, 100, 107, 113-115]. Before the electrophoretic deposition process was performed, the new electrolyte suspensions were vigorously mixed for 1 hour, to fully disperse the composite materials. The names of the coated scaffolds derived with each type of electrolyte suspension are also listed in table 3.

A pre-selection study based on cytotoxicity was performed to find the most promising concentration of the (nano-)materials in the electrolyte suspension, since the effects of these materials are strongly dose-dependent [82-84]. Each concentration was analysed using a quantitative Alamar Blue assay and a qualitative Live/dead assay, which are later described in more detail. For the reason of simplicity, the scaffolds coated with the selected electrolyte suspensions were afterwards renamed (table 3).

Composition electrolyte suspension	Name group	Name selected group
n/a	ASM	ASM
0.5 g/l chitosan	CH	CH
0.5 g/l chitosan + 0.05 g/l nSi	Si-1	
0.5 g/l chitosan + 0.25 g/l nSi	Si-2	
0.5 g/l chitosan + 1.0 g/l nSi	Si-3	Si
0.5 g/l chitosan + 0.1 g/l nHA	HA-1	
0.5 g/l chitosan + 0.5 g/l nHA	HA-2	
0.5 g/l chitosan + 2.0 g/l nHA	HA-3	HA
0.5 g/l chitosan + 0.05 g/l SrCl	Sr-1	
0.5 g/l chitosan + 0.25 g/l SrCl	Sr-2	Sr
0.5 g/l chitosan + 1.0 g/l SrCl	Sr-3	
0.5 g/l chitosan + 0.05 g/l GO	GO-1	
0.5 g/l chitosan + 0.2 g/l GO	GO-2	
0.5 g/l chitosan + 0.5 g/l GO	GO-3	GO

Table 3: Composition electrolyte suspension of experimental groups

2.5 Surface characterization

Microscopical pictures were made (directly after coating) using a LEICA ICC60 W.

2.5.1 Topography

Micro-scale pictures of the topography of the ASM, CH, and the selected composite groups were obtained using a scanning electron microscope (SEM), specifically a JEOL (JSM-6500F, Tokyo, Japan). Before analysis a nano-layer of gold was sputtered on the surface to provide the essential conductive layer on top of the non-conductive coated samples.

2.5.2 Local Surface chemical composition

During SEM imaging the local surface chemical composition was analysed using energy dispersive X-ray spectroscopy (EDS) (JEOL JSM-6500F). $K\alpha$ X-ray counts were collected from point scans at fairly flat locations of the scaffold's surface. The atomic composition of the surface was acquired by normalizing the height of the element specific peaks to the total height.

2.5.3 Thickness & degradation

In order to assess the initial coating thickness and the degradation behavior, one coated scaffold for each of the selected groups of Si, HA, Sr, and GO, was directly analyzed using a combination of focused ion beam (FIB) and scanning electron microscopy (SEM) (FEI Strata Dual-beam FIB & JEOL JSM-6500F). A second scaffold was incubated (37 ± 0.5 degrees Celsius) for one month (31 days) in PBS prior to analysis. Afterwards the samples were dried overnight and analyzed by SEM.

2.5.4 Release profile

Three coated scaffolds ($n=3$) for each of the selected Si, HA, and Sr groups were incubated (37 ± 0.5 degrees) in 10ml of PBS. At different time points: 4 hours, day 1, day 3, day 7, and day 14, the PBS was

replaced, a small amount of nitric acid was added (0.6%), and stored at 4 degrees. The samples were analysed using inductively coupled plasma optical emission spectrometry (ICP-OES)(Spectro Arcos). Table 4 summarizes the different ion concentrations which were assessed. The ion release of the samples was corrected based on the concentrations found in the PBS. The cumulative release profile of the samples was realized by combining the data of all time-points.

Group	Ion types
Si	Si^{4+}, Li^+, Mg^{2+}
HA	Ca^{2+}, P^{5+}
Sr	Sr^{2+}

Table 4: Ion types release profile

2.6 Cell culturing & sterilization

All in vitro assays were conducted using a MC3T3 pre-osteoblast mouse cell line [116] (ATCC, Germany). The culture medium consisted of alpha-MEM medium (Invitrogen, USA) supplemented by 10% fetal bovine serum (Cambrex, USA), and 1% antibiotics (penicillin/streptomycin, Invitrogen, USA). All cells were incubated at 37 ± 0.5 degrees Celcius, 5% CO₂, during culture. Cell seeding density was determined by pilot experiments to avoid cell overgrowth and set at 200.000 cells per sample for assessment of seeded scaffolds, and 20.000 cells per sample for monolayer experiments.

All scaffolds used for in vitro assays were sterilized by exposure to high intensity ultraviolet light (CL-1000 Ultraviolet Crosslinker) on both sides for 15 min.

2.7 Cell viability & Cytotoxicity

In order to evaluate the effect on cell viability of the coated samples on both attached cells and cell monolayers via the release of elements, separate cell viability experiments were conducted. Figure 5 [81](edited), provides a schematic overview of the different experiments.

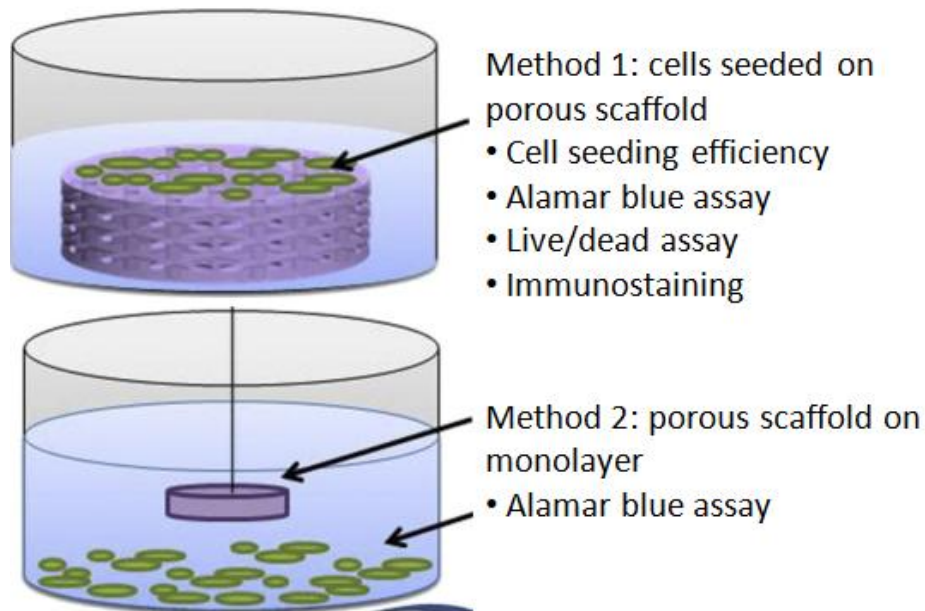


Figure 5: Cell viability & cytotoxicity experiments

2.7.1 Cell seeding efficiency

The cell seeding efficiency was performed to elucidate the effect of the different coatings on the cell seeding. At day 1, after seeding the samples at day 0, the cell seeding efficiency was assessed by measuring the amount of DNA derived from the attached cells on the samples and the DNA from the cells on the bottom of the well plate separately. A pico green assay was used to evaluate the amount of DNA. First the scaffolds were moved to separate wells, after which both the attached cells on the scaffolds and the remaining cells attached cells at the well bottom were lysated (non-adherent dead cells were removed by washing). Pico green reagent (0.5%) was added to each lysate. After 5 min of incubation in the dark, the fluorescence was measured between 485 nm and 520 nm using a micro-plate reader (Fluoroskan Ascent FL, Thermo Fisher Scientific). A standard curve was made by analysis of known concentrations of DNA following the same procedure.

2.7.2 Attached cells viability & cytotoxicity

For the experiments on attached cells, cells were seeded (pipetted) on top of the scaffolds and incubated at day 0 of the experiments. At day 1 the samples were transferred to a new well, only bringing the attached cells. Qualitative assessment of cytotoxicity was performed using a live/dead assay and by immunostaining. Quantitative assessment was performed by evaluating the metabolic activity via an Alamar Blue (Resazurin) assay. The Alamar Blue assay was conducted at day 1, day 3, and day 7, for

all experimental groups. 10% of resazurin (440mM) was added to the normal culture medium of the samples, followed by 4 hour incubation in the dark. Afterwards the absorbance was analysed using a Fluoroskan Ascent FL reading between 544 and 570 nm (Thermo Fisher Scientific).

Live/dead assay was executed at day 2 using one sample for each experimental group. Cells were stained with Ethidium homodimer (0.1%) and Calcein AM (0.05%) during 30 min of incubation in the dark. The analysis was conducted with a fluorescence microscope (Olympus BX51, Japan). The pictures from both the red (dead cells) and green (living cells) domain were combined using Photoshop CC (Adobe).

Immunostaining of the cell body and the nucleus was performed at day 1 for the selected experimental groups. Cells were stained using mouse monoclonal antivinculin (0.125%) for 1 hour at 37 degrees Celsius and Dapi (1%) 5 minutes in the dark. Fluorescence microscopy was used to analyze the samples (Olympus BX51, Japan). Pictures from both domains (stainings) were later combined using using Photoshop CC (Adobe).

2.7.3 Monolayer viability & cytotoxicity

For the monolayer experiment, a monolayer of cells was seeded and incubated for one day before the start of the experiment. At day 0 of the experiment sterile scaffolds were gently placed on top of the monolayer. Alamar blue assay was conducted at day 1, day 3, and day 7, following the same protocol as provided in 2.7.2, to evaluate the viability of the cells surrounding the scaffold.

2.8 ALP activity

Intracellular alkaline phosphatase (ALP) activity of three samples of each selected group (n=3, no GO) was measured, at day 1, day 7, and day 14, to assess osteoblast activity. At these time points, all attached cells were lysated using a specially designed plate, in which the scaffolds could be fully submerged in 200 ml of lysis buffer (0.2% Triton-x 100, PBS). After 30 minutes, p-nitrophenyl phosphate (tablets, Sigma-Aldrich, Germany) was added to each sample, according to the manufacturers protocol, followed by 30 min incubation in the dark. The samples were analysed using a fluorescence plate reader (VersAmax tunable, Molecular Devices, USA), measuring between 405 nm and 655 nm. A standard curve was made by analysis of known concentrations of calf intestinal ALP following the same procedure.

2.9 Osteogenic differentiation

The effect of composite coatings on osteogenic differentiation was assessed by quantitative real-time polymerase chain reaction (qPCR). At day 1, day 11, and day 21, three samples for the selected groups (n=3, no GO) were placed in Trizol reagent (Ambion), and the RNA was extracted using a RNA extraction kit (Qiagen). Hereafter copy DNA (cDNA) was made using the RNA and a cDNA synthesis kit (Fermentas). The level of expression of several osteogenic gene markers was quantified using Sybr Green primers in a Light Cycler 96 (Roche). The following osteogenic gene markers were analysed: runt-related transcription factor-2 (Runx2), alkaline phosphatase (ALP), osteocalcin (OCN), bone sialoprotein (BSP), vascular endothelial growth factor (VEGF), and osteopontin (OPN). All expression levels were normalized based on the expression level of the house keeping gene glyceraldehyde 3-phosphate dehydrogenase (GAPDH).

2.10 Antibacterial effect

The antibacterial effect of the selected experimental groups was investigated on both adherent and planktonic *Staphylococcus aureus* (ATCC 29213). First bacteria were grown on blood agar plates and incubated (37 degrees) over night. Subsequently, the bacteria were cultured in tryptic soy broth (TSB) medium (1% glucose) at 37 degrees for 18 hours. Afterwards the bacteria suspension was diluted to optical density (OD) 600 0.01. Scaffolds were placed in 48 wells plate and immersed in 600ul of the diluted bacteria solution at the day 0 time point.

2.10.1 CFU

The antibacterial effect of the coatings was evaluated based on both adherent (bio-film) and planktonic bacteria. At day 1, both the number of adherent bacteria and the planktonic bacteria in the medium was measured by counting the number of colonies using serial dilution. The planktonic bacteria were directly derived from the medium, and counted. Before counting the adherent bacteria, the samples were washed in phosphate buffered saline (PBS) thrice to remove all nonadherent bacteria. Subsequently, the samples were sonicated for 1 minute in 2 ml PBS, to loosen the adherent bacteria, after which the colonies were counted using serial dilution.

2.10.2 SEM

After 1 day of bacteria culturing one sample for each selected group was assessed by SEM. The samples were first three times washed with PBS, followed by fixating by 2% glutaraldehyde (4 degrees Celsius, 2 h). Subsequently, a dehydration process was conducted by immersion in consecutively 3 ml of: 25% and 50% ethanol-PBS, 75% and 90% ethanol-water, two times 100% ethanol, 50% ethanol-hexamethyldisilazane and 100% hexamethyldisilazane. Finally, after drying the samples overnight, the surface of the samples were gold-sputtered (1.7 nm in thickness) prior to SEM imaging. Micro-scale pictures of the topography and attached bacteria were obtained using a JEOL scanning electro microscope (JSM-6500F, Tokyo, Japan)

2.11 Statical analysis

Statistical differences between the experimental groups were assessed using one-way ANOVA and Tukey-Kramer posthoc tests.

3. Results

3.1 Particle size distribution

All four (nano-)materials were assessed by DLS. The result of the silicate nano-powder can be found in (fig. 6). The highest intensity was observed for a hydrodynamic diameter of 67.49 nm. The other materials could not be properly analysed by DLS. For both hydroxyapatite nano-powder, and graphene oxide, the observed light scattering was too noisy to correlate to the hydrodynamic diameter. In case of the strontium chloride powder, the detected light scattering was below the threshold value.

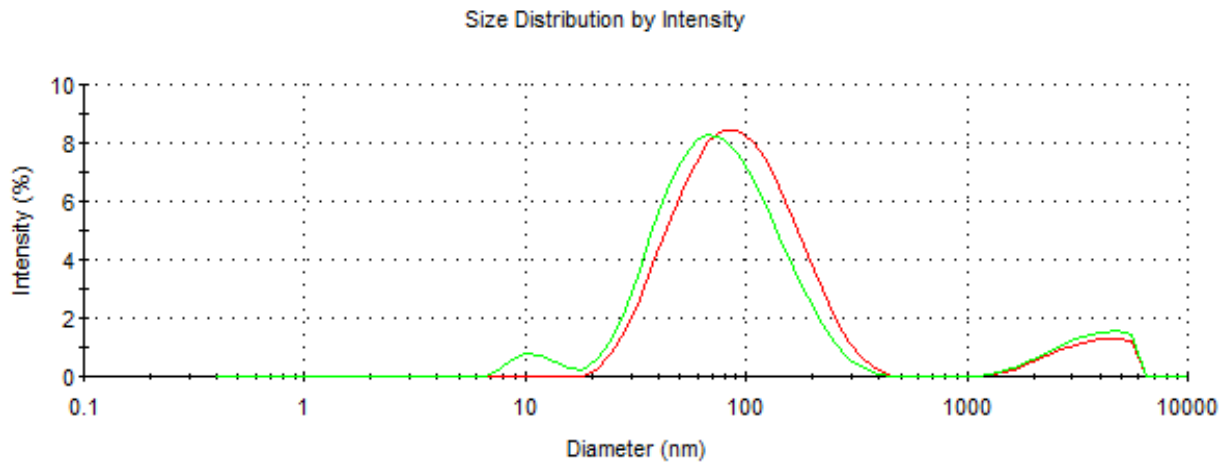


Figure 6: Particle size distribution of silicate nano-powder of two consecutive DLS runs (red & green)

3.2 Zeta potential

Table 5, shows the zeta potential values of the EPD suspensions. The pure chitosan EPD suspension was strongly positively charged: $+64.3 \pm 1.9$ mV. All suspensions showed zeta potential values of (approximately) above +30 mV. The addition of (nano-)materials to the chitosan suspension seemed to decrease the zeta potential, especially at higher concentrations.

Group	Zeta potential (mV)
CH	$+ 64.3 \pm 1.9$
Si 1	$+ 54.0 \pm 0.8$
Si 2	$+ 58.3 \pm 0.6$
Si 3 (Si)	$+ 37.2 \pm 2.3$
HA 1	$+ 56.3 \pm 0.7$
HA 2	$+ 48.4 \pm 1.3$
HA 3 (HA)	$+ 42.3 \pm 0.5$
Sr 1	$+ 58.0 \pm 1.4$
Sr 2 (Sr)	$+ 38.8 \pm 1.6$
Sr 3	$+ 40.4 \pm 2.1$
GO 1	$+ 43.3 \pm 4.8$
GO 2	$+ 30.0 \pm 1.3$
GO 3 (GO)	$+ 35.9 \pm 1.0$

Table 5: Zeta potential of EPD suspensions

3.3 Topology

Figure 7A displays the microstructure of the ASM scaffold, clear signs of the selective laser melting process can be observed in the form of the spherical powder like agglomerations near the curvatures. Surface features of respectively, CH, Si, HA, Sr, and GO, can be observed in figure 7B-F. The presence of a (composite) coating, often characterized by small cracks, is observable at all coated surfaces (fig. 7 B-F). The dominant structure of the graphene oxide sheets is clearly visible at the GO surface (fig. 7F).

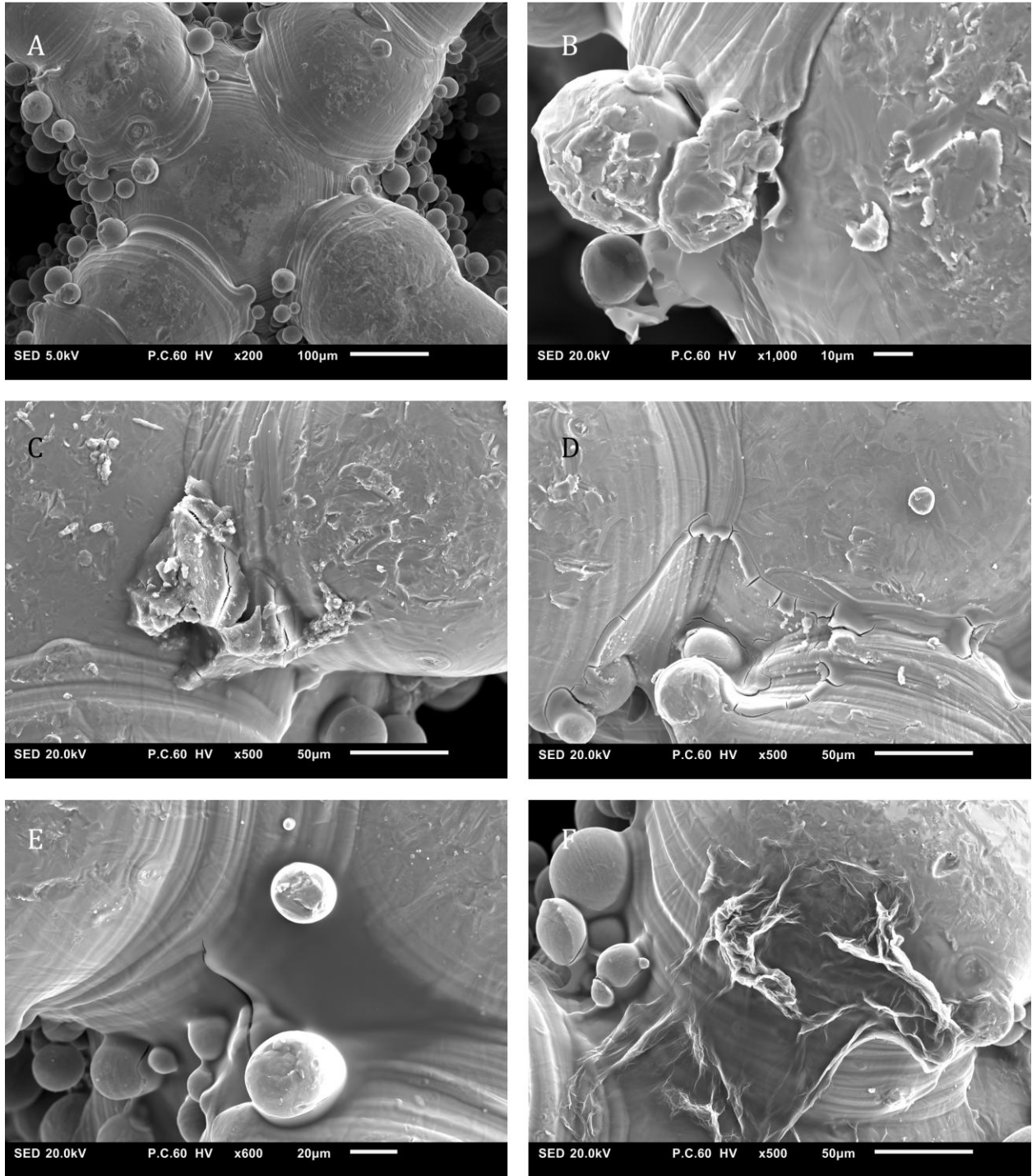


Figure 7: SEM images of (A) ASM, (B) CH, (C) Si, (D) HA, (E) Sr, (F) GO

Attempts to measure the coating thickness are shown in figure 8 A,B (CH). First, a smooth rectangular hole was burned in the scaffold surface. Afterwards the coating thickness could be analysed by tilting the sample 45 degrees (A,B). This specific measurement showed a thickness of around 1.1 μm (B). However, due to surface irregularities, and high variance in thickness, it was not possible to find an accurate value for the thickness of both the fresh coatings and the degraded coatings. Assumptions based on naturally occurring cracks in the coating (C,D) point towards a fresh coating thickness of around 2 μm .

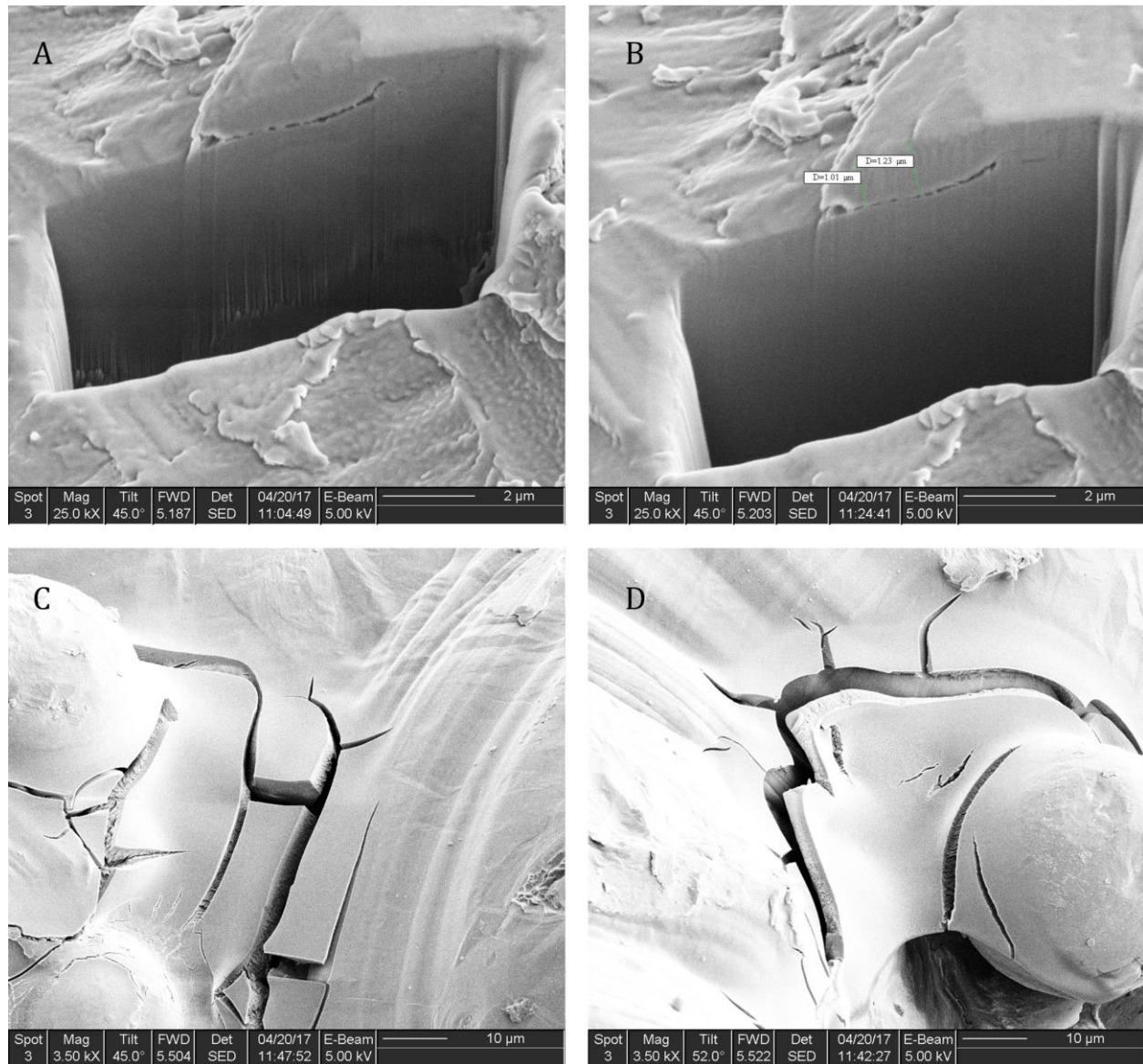


Figure 8: SEM images of (A) FIB location (B) Thickness measurement at FIB location (C,D) Cracks in the chitosan coating

3.3.1 Local surface chemical composition

Table 6 summarizes the local surface chemical compositions found by EDS at the location of the SEM pictures. The ASM surface predominately consists of titanium with a small amount of oxygen. The CH-coating surface consists of oxygen, carbon, and nitrogen, besides titanium. These elements are associated with chitosan and affirm the presence of a chitosan coating. The Si surface consists of high percentages of silicium and magnesium together with the chitosan associated elements, which validates successful co-deposition of both components. Chitosan's presence can also be found in the surface composition of HA. Furthermore, calcium and phosphor, the two main components of hydroxyapatite, were successfully deposited. The presence of strontium (and chloride) was validated at the Sr surface. Clear signs of chitosan could also be found. Finally, The GO surface displays elevated amounts of carbon and oxygen when compared to the CH surface. This validates the presence of both graphene oxide and chitosan.

#	Ti (wt%)	O (wt%)	C (wt%)	N (wt%)	Sr (wt%)	Cl (wt%)	Ca (wt%)	P (wt%)	Si (wt%)	Mg (wt%)
ASM	97.54	2.46								
CH	47.4	29.26	20.53	2.8						
Si	6.73	33.06	17.31	3.03					28.38	11.48
HA	12.23	51.63	12.47	0.91			12.07	10.7		
Sr	47.4	36.98	14.24	0.71	0.29	0.82				
GO	2.77	51.49	43.87	1.87						

Table 6: Local surface chemical composition measured by EDS

3.4 Release profile

The release profiles in the first two weeks can be observed in figure 17 Si clearly released silicium, Lithium, and magnesium ions (fig. 17 A,B,C). The release profiles all show a high burst release: approximately 50% during the first 4 hours and 50% during the remaining two weeks. The lithium concentrations at most later time points were non-detectable. HA (burst) released calcium and phosphorus ions during its degradation (fig. 17 D, E). Finally, Sr released strontium ions with a high burst during the first hours: approximately 70% during the first 4 hours and 30% during the remaining 14 days (fig. 17 F). All assessed released profiles showed a low variance between the different samples of the same groups.

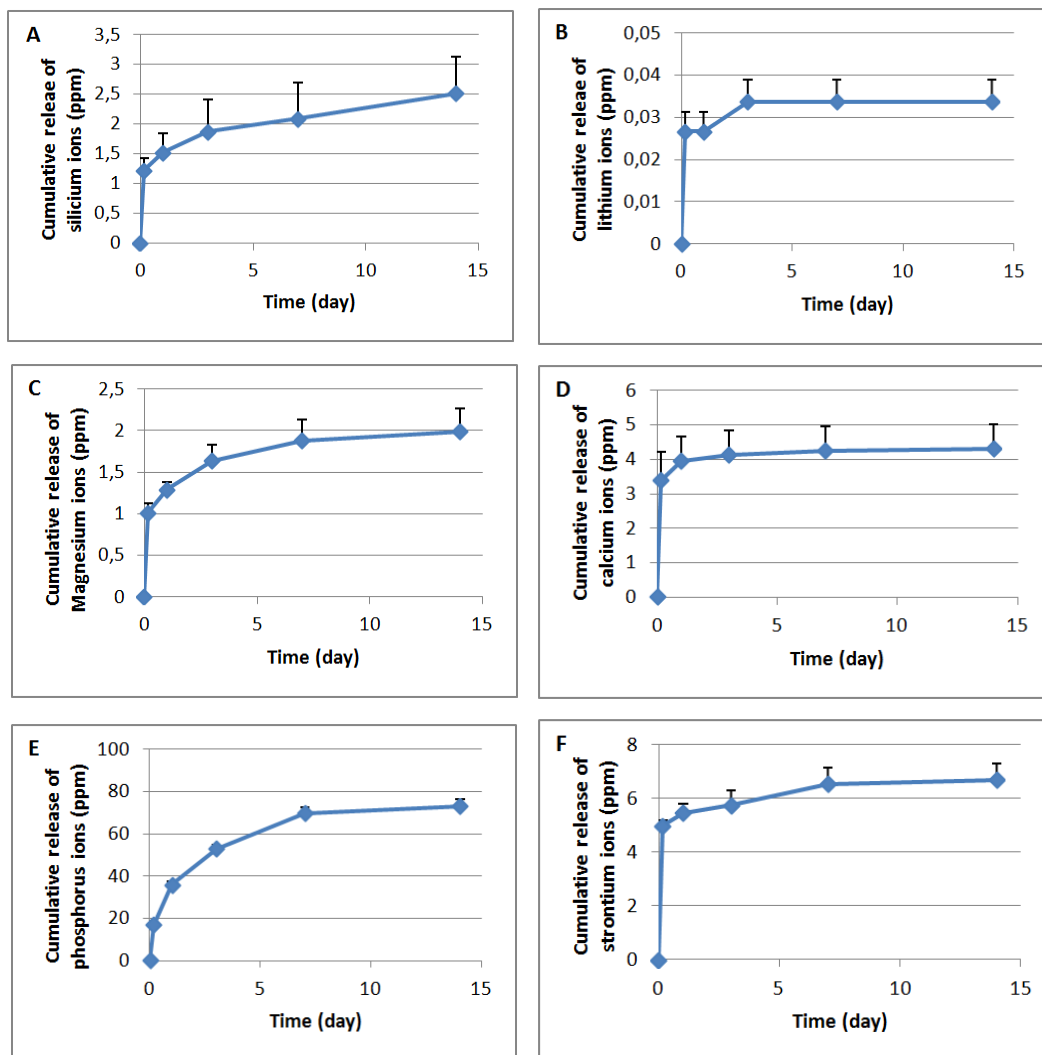


Figure 9: Cumulative release profile of: **Si**: (A) Silicium ions, (B) Lithium ions, (C) Magnesium ions; **HA**: (D) Calcium ions, (E) Phosphorus ions; **Sr**: (F) Strontium ions

3.5 Pre-selection study

3.5.1 Si

The Alamar Blue assay did not provide statistically significant differences on the investigated time points (fig. 10). However, it can be observed that the absorbance of Si3 has the highest absorbance at each time point (day 1, day 3, day 7). Similarly, the Live/dead assay (day 2) showed a comparable rate of cytotoxicity for each concentration (fig. 11). Finally, Si3 was chosen for further analysis based on the potentially better long term results.

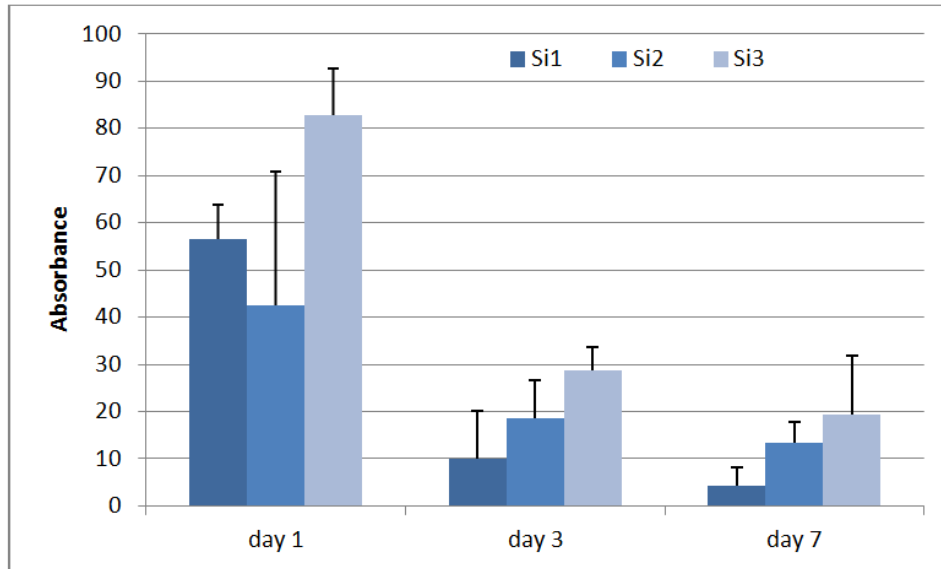


Figure 10: Alamar Blue assay day 1, day 3, day 7

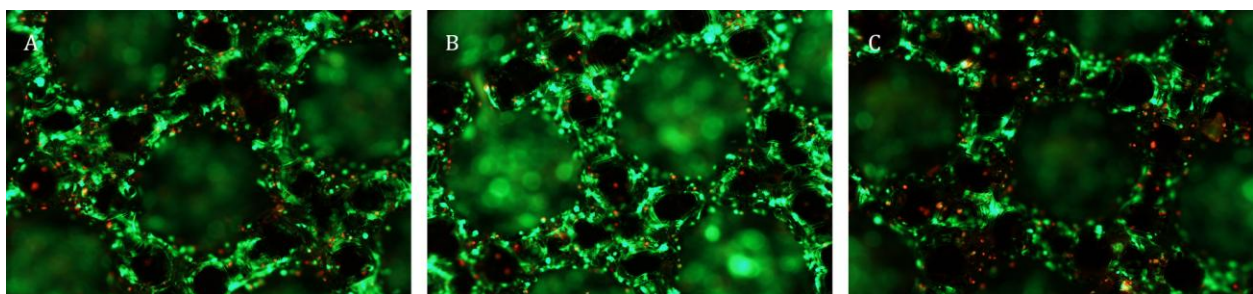


Figure 11: Live/dead images of (A) Si1, (B) Si2, (C) Si3

3.5.2 HA

At day 1 and day 3 of the Alamar Blue assay (fig. 12) the HA3 showed the highest absorbance (not statistically significant). At day 7, both HA1 and HA3 performed significantly better than HA2 which effectively did not perform better than the negative control (culture medium). The Live/dead assay (fig. 13) showed comparable results for HA2 and HA3, where HA1 showed a greater number of both viable cells and dead cells. To conclude, HA3 was chosen and further evaluated.

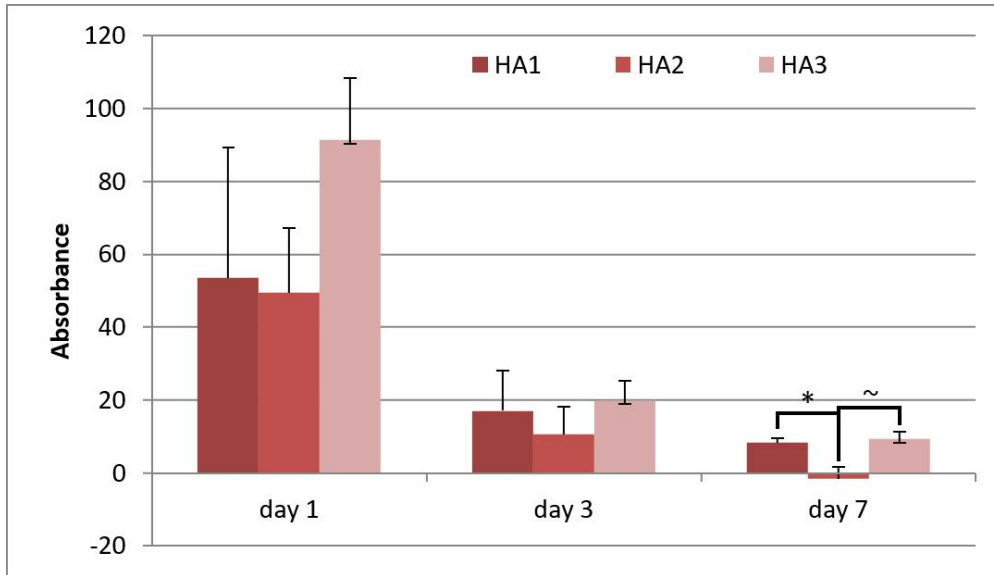


Figure 12: Alamar Blue assay day 1, day 3, day 7

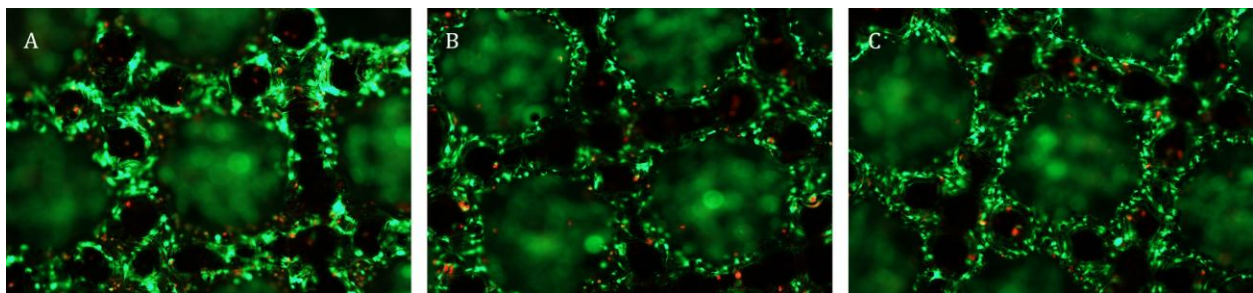


Figure 13: Live/dead images of (A) HA1, (B) HA2, (C) HA3

3.5.3 Sr

No statistically significant differences were observed at the day 1 and day 3 time point of the Alamar Blue assay (fig.14). At day 7, both Sr1 and Sr2 were significantly better performing than Sr3. The Live/dead assay showed the least cytotoxicity Sr2 (fig. 15). Especially the surface of Sr1 contained a great number of dead cells . Sr2 was chosen for further investigation.

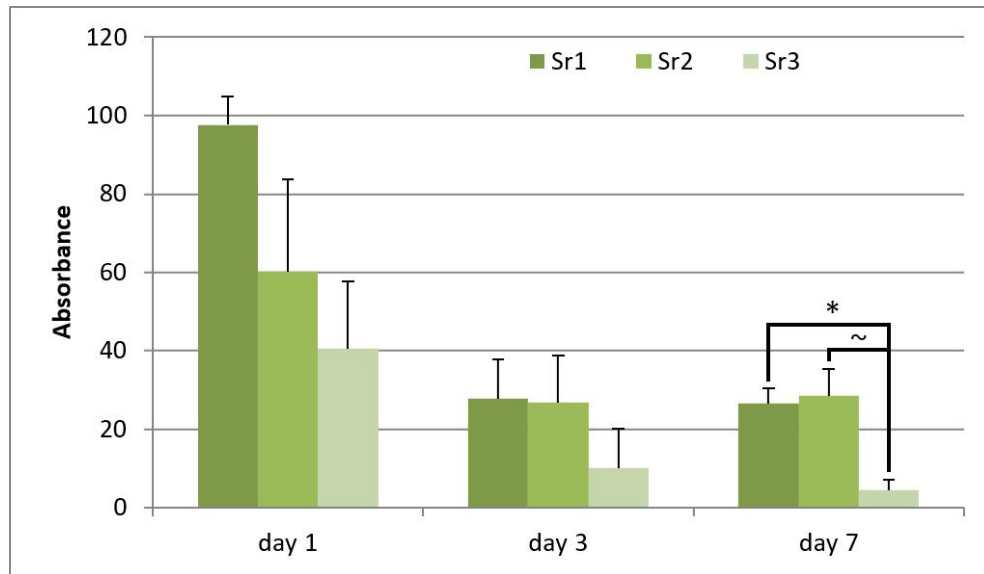


Figure 14: Alamar Blue assay day 1, day 3, day 7

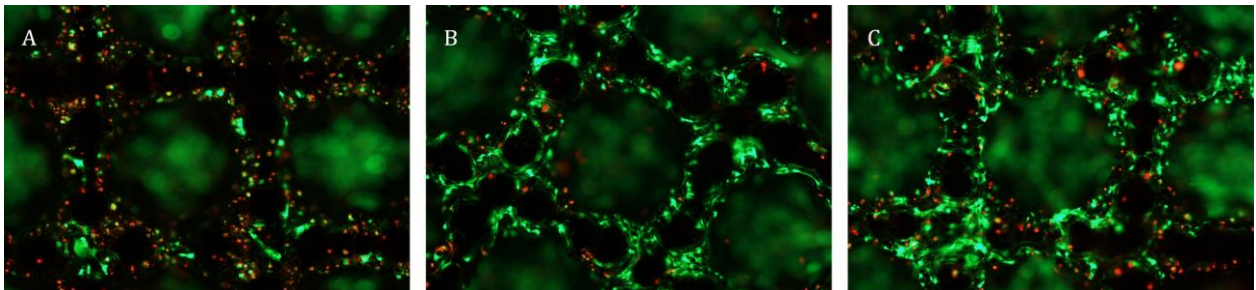


Figure 15: Live/dead images of (A) Sr1, (B) Sr2, (C) Sr3

3.5.4 GO

At day 3 and day 7 of the alamar blue assay, the GO3 showed a significant higher metabolic activity than the other concentrations (fig. 16). This trend was also observed during the Live/dead assay at day 2: GO3 showed fewer dead cells and a greater number of living cells (fig. 17). Ultimately, GO3 was picked for further analysis.

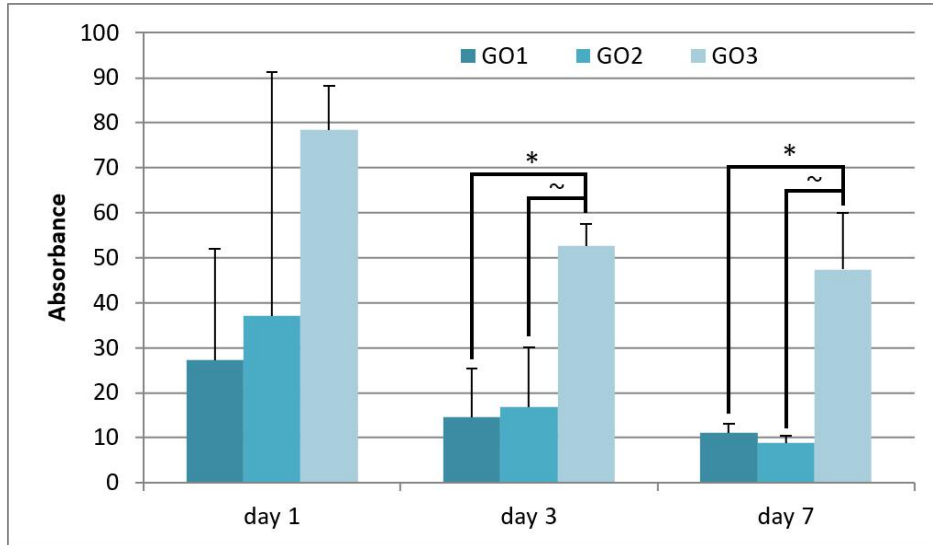


Figure 16: Alamar Blue assay day 1, day 3, day 7

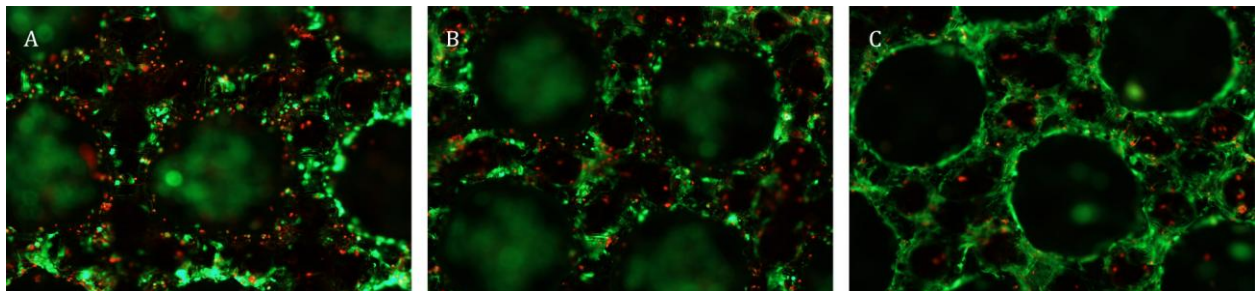


Figure 17: Live/dead images of (A) GO1, (B) GO2, (C) GO3

3.6 Antibacterial effect

The antibacterial properties of the selected groups against both planktonic and adherent bacteria were evaluated. The presence of adherent bacteria, which are responsible for the production of biofilm, was qualitatively assessed with SEM (fig. 18) and quantitatively with a CFU assay (fig. 19). SEM imaging of bacteria showed that all scaffolds are colonized by a considerable number of bacteria. The CH-scaffold (fig. 18 B) seems to carry the least number of bacteria, followed by the Sr- and ASM-scaffolds (fig 18. E, A). The Si- and HA-scaffolds (fig 18. C,D) show clear signs of formation of biofilm and seem to increase the bacteria adhesion compared to the ASM-scaffold. Unfortunately, the sputtered gold layer was slightly thicker at the Sr-scaffold, which partially buried the bacteria.

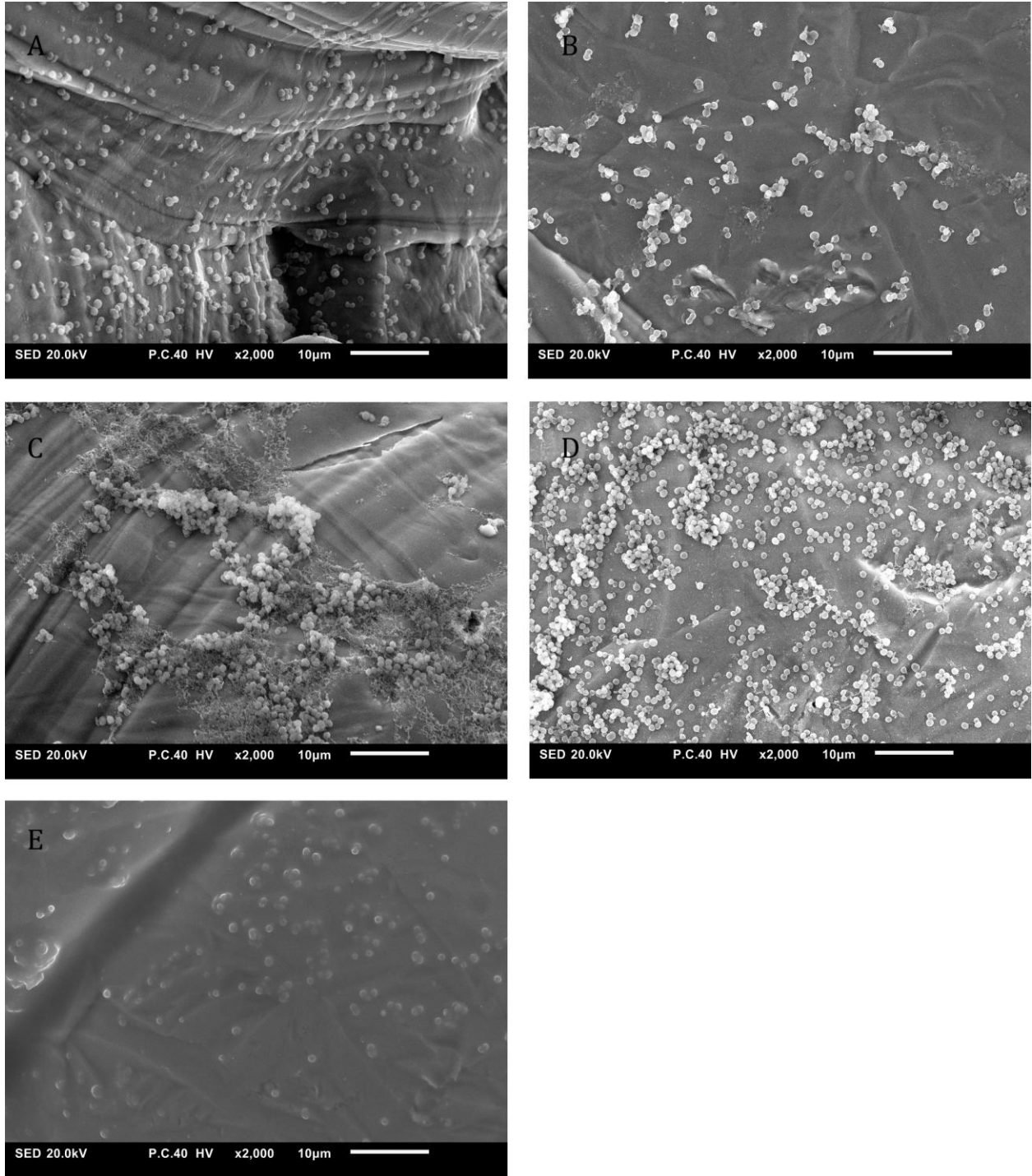


Figure 18: SEM images of bacteria (A) ASM, (B) CH, (C) Si, (D) HA, (E) Sr

The CFU assay at day 1 did not result in significant differences between the groups, although the coated scaffolds, especially CH, seems to lower the number of attached bacteria (fig. 19).

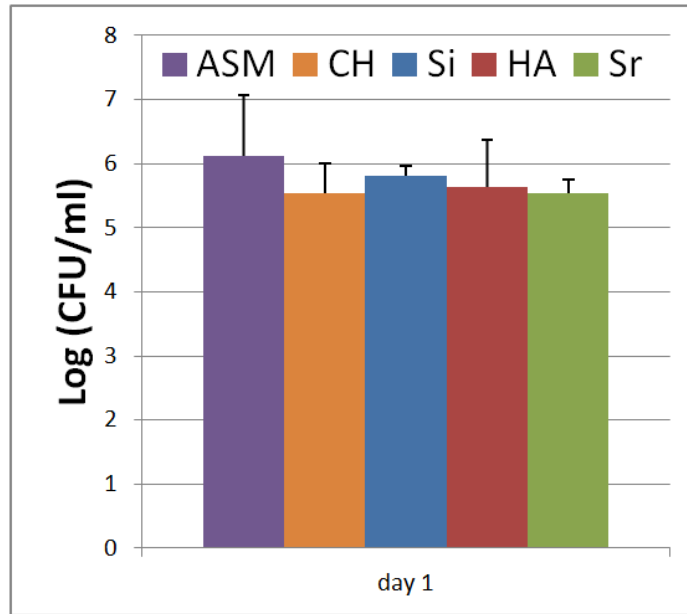


Figure 19: CFU Assay adherent bacteria (biofilm)

Similarly, the CFU assay conducted with planktonic bacteria, did not show significant differences between the groups (fig. 20). The positive control (bacteria without a scaffold) showed comparable values (Log(CFU) \approx 9).

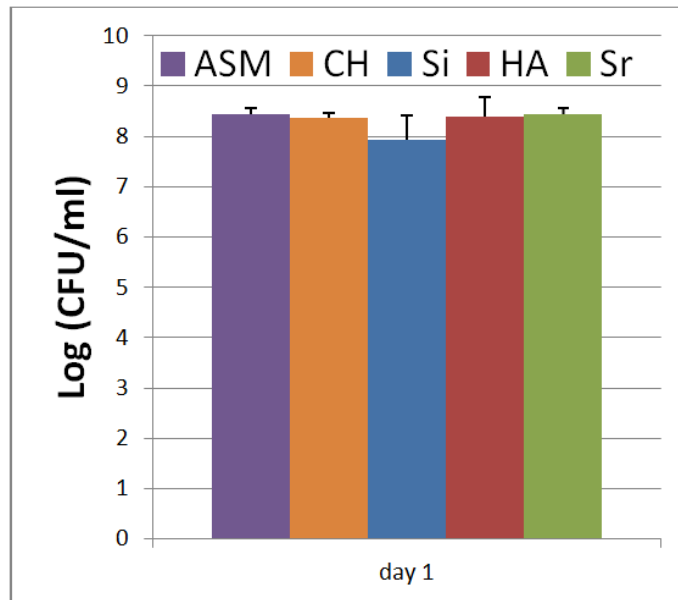


Figure 20: CFU Assay planktonic bacteria

3.7 Cytotoxicity

The CSE assay, conducted at day 1, found a clear significant difference between ASM and CH scaffolds (fig. 21 A). The composite coatings seem to improve the CSE compared to CH, but still perform worse than ASM. The DNA content of the cells attached to the well bottom did not show significant differences between groups (fig. 21 B). The total DNA content, scaffold plus well bottom, seemed to be quite similar for all groups.

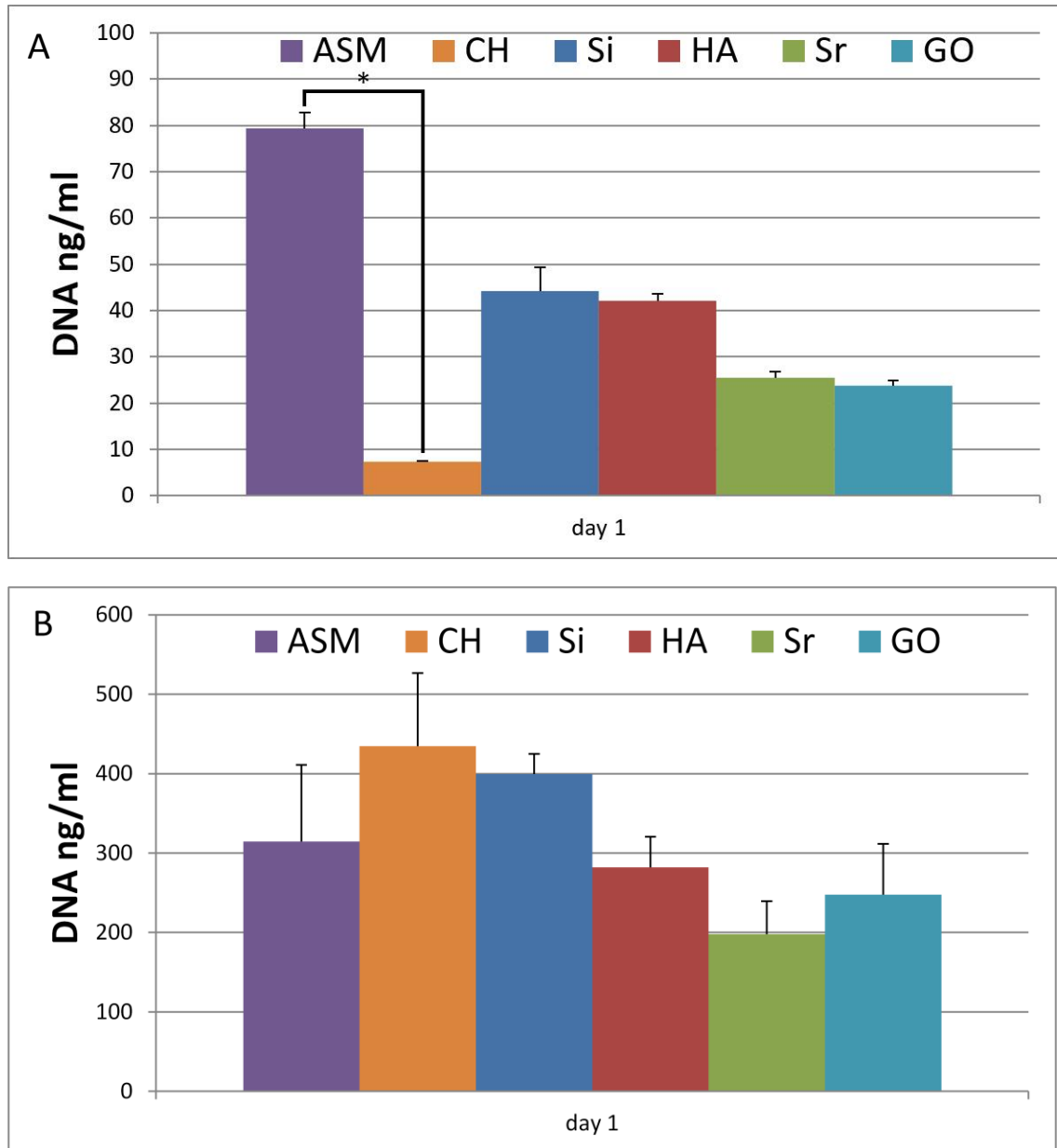


Figure 21: CSE (A) CSE scaffold (B) DNA content well bottom

The results of the Alamar Blue assay conducted on attached cells can be found in figure 22 . At the day 1 and day 3 time point ASM significantly outperformed the coated samples. At day 7 no significant differences were found, as the difference between the coated scaffolds , especially GO, and ASM decreased.

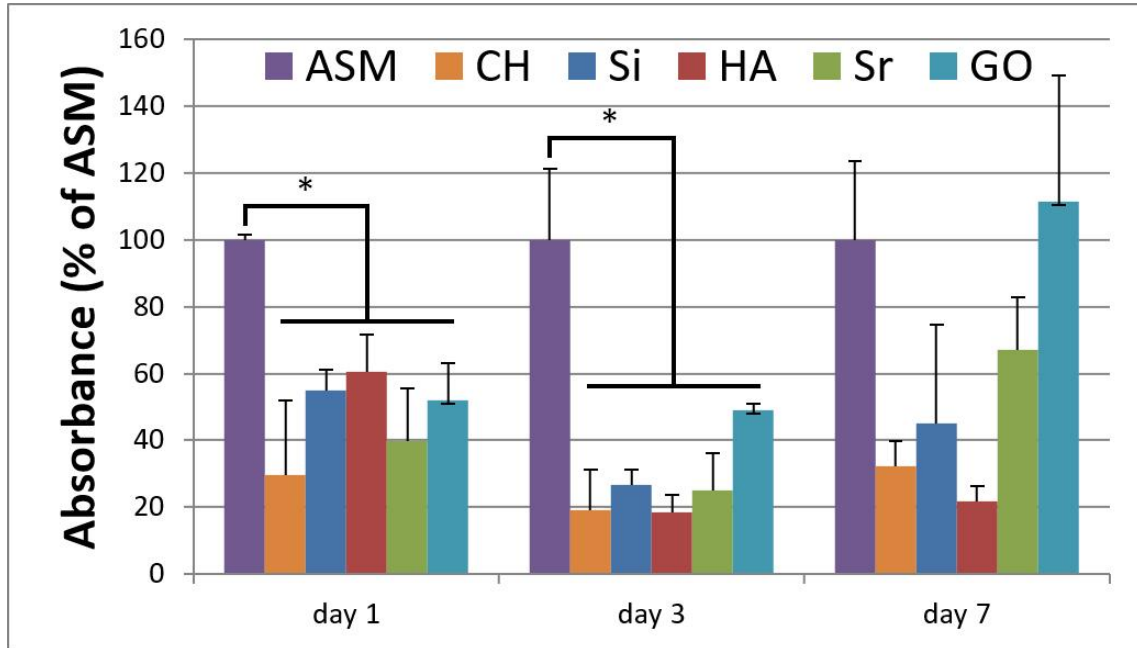


Figure 22: Alamar Blue assay attached cells day 1, day 3, day 7

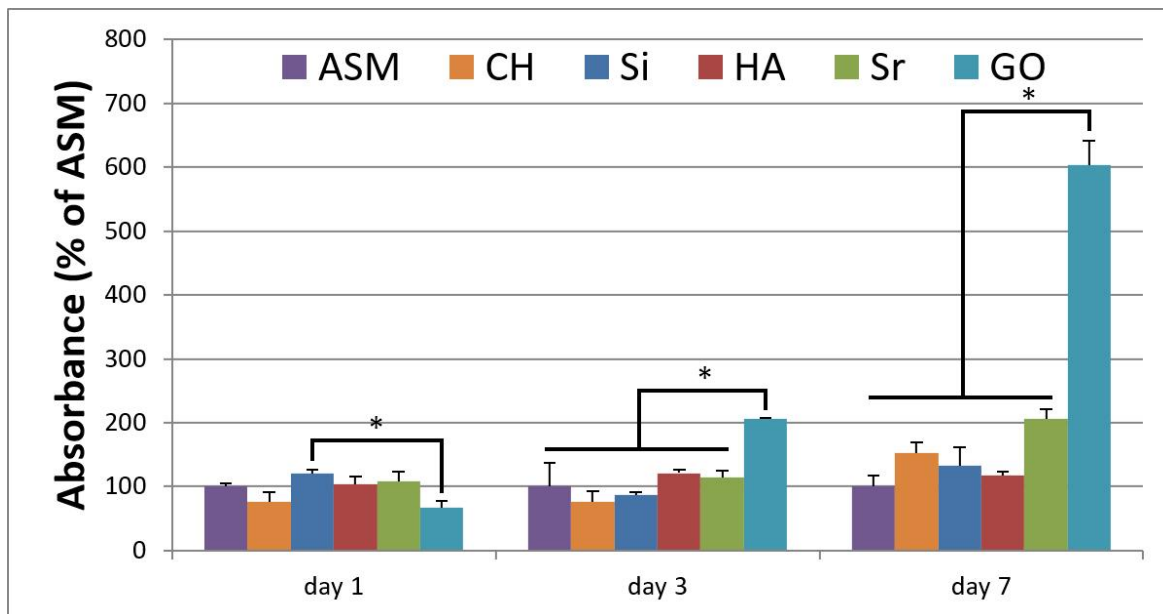


Figure 23: Alamar Blue assay monolayer day 1, day 3, day 7

The Alamar Blue assay conducted on a monolayer of cells showed similar cell viability for ASM, CH, Si, HA, and Sr (fig. 23). At day 1, HA showed a significant higher metabolic activity than GO. At day 7, and especially day 14, GO showed a significant increase in metabolic activity compared to all other groups, rising to a 6 times higher value than ASM at day 14.

3.8 ALP activity

The ALP activity measurements did not result in significant differences at the day 1, day 7, and day 14 time points (fig. 24). Moreover, the ALP activity of the (composite) coated scaffolds showed great similarity at all investigated time points.

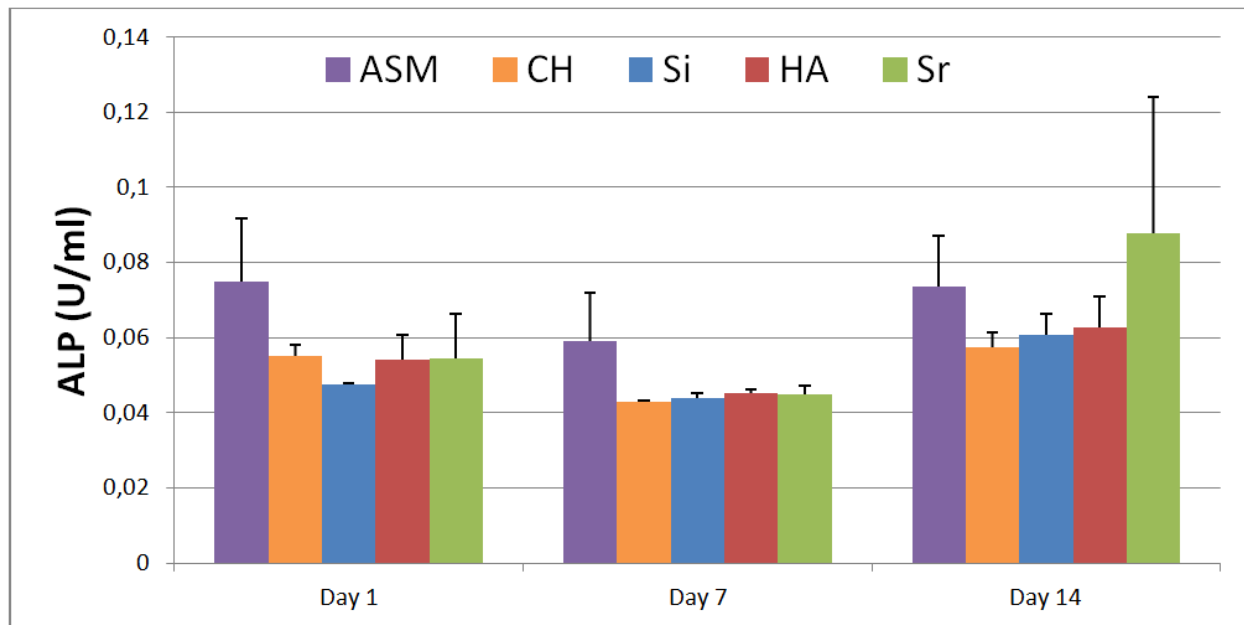


Figure 24: ALP activity day 1, day 3, day 7

3.9 Cell morphology

Nucleus (blue) and cell body (green) were stained and visualized at the day 1 time point (fig. 25). Interestingly, the initial attachment of cells seems to be highest at the CH-coated scaffold (fig. 25 B). The composite coated scaffolds (fig 25 C, E, F) seem to slightly decrease the number of attached cells when compared to the ASM scaffold (fig. 25 A). The morphology of the cell bodies could not be assessed based on the acquired images. Partial overlapping and surface curvature made it impractical to discriminate between the stretched (healthy) and compact (unhealthy) cell morphologies.

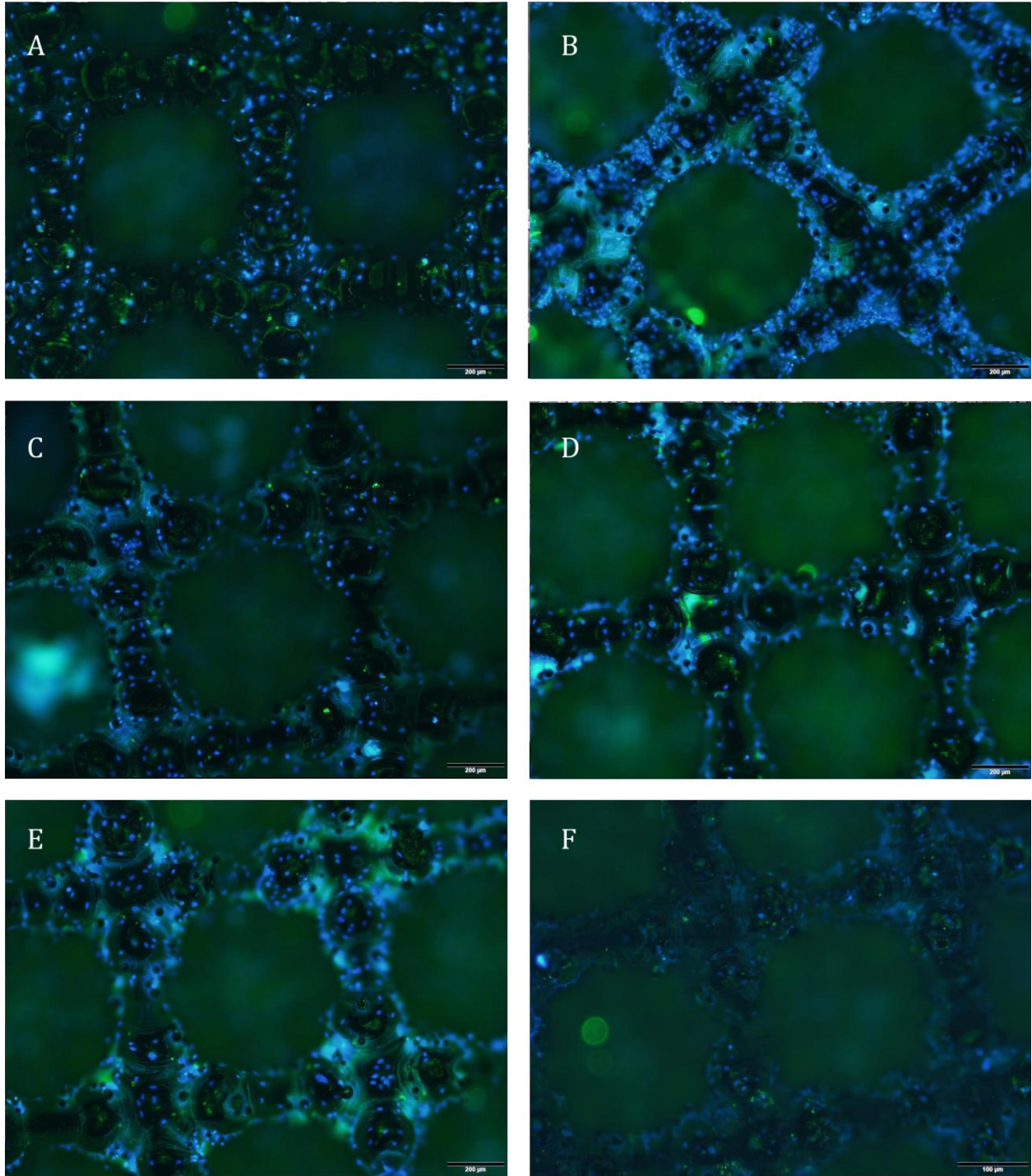


Figure 25: Immunostaining (A) ASM, (B) CH, (C) Si, (D) HA, (E) Sr, (F) GO

3.10 Gene expression

The amount of harvested RNA was relatively low for some of the sample. As a result, the expression of some of the genes was undetectable by qPCR. More specifically, the samples harvested at the day 1, and day 11 time points, were affected by this problem. Table 7 shows the percentages of samples with undetectable gene expression for each group and time point. Since three samples per group and time point were prepared, a few unanalysable samples per group made the data of the day 1 and day 11 time points unreliable in terms of variance, significant differences, and standard deviation. The gene expression of the day 21 samples, which were not affected by the aforementioned problems, are shown in figure 26. No statistically significant differences between the groups were observed.

Group	Day 1	Day 11	Day 21
ASM	33%	19%	0%
CH	71%	14%	0%
Si	33%	33%	0%
HA	29%	19%	0%
SR	43%	24%	0%

Table 7: Percentage of unanalysable samples by qPCR

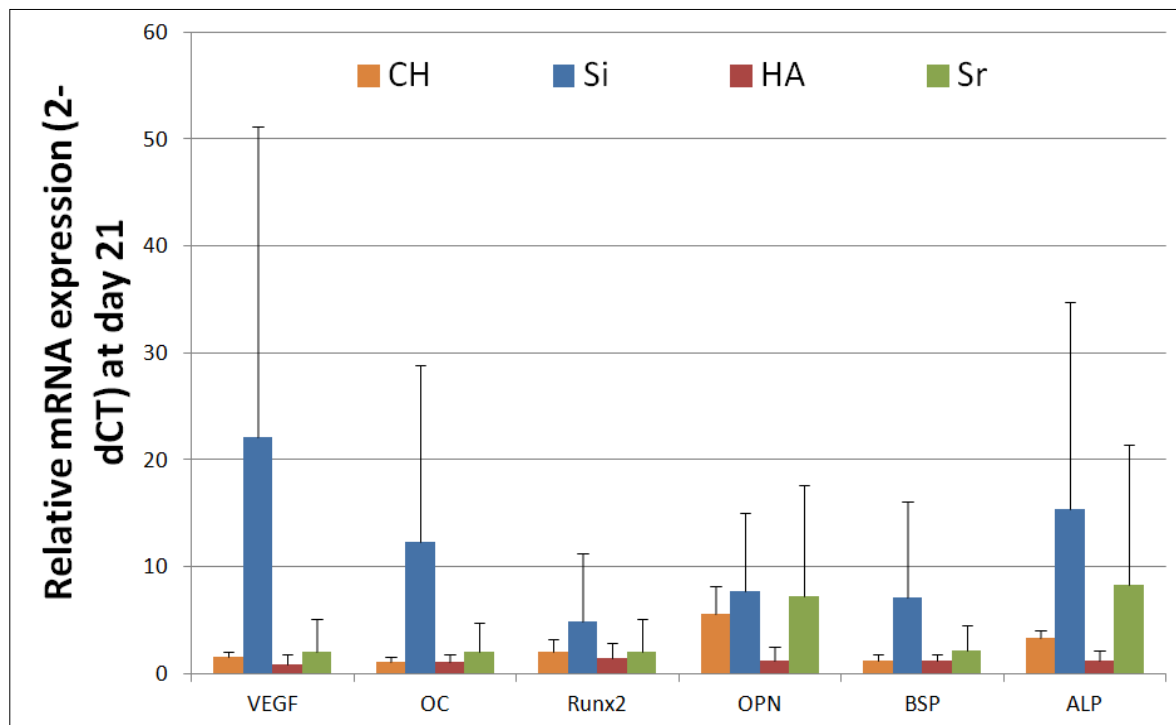


Figure 26: Expression of VEGF, OCN, Runx2, OPN, BSP, and ALP, normalized to ASM at day 21

4. Discussion

4.1 Material characterization

The reliability of DLS, which measures the particle size distribution via laser scattering by particles, depends on an equal particle size distribution [117]. Larger particles or aggregations of smaller particles scatter more light than smaller particles. As a result, smaller particles are overshadowed by larger particles in the measurement data when there is a high variance in particle size. Both graphene oxide and nano-hydroxyapatite powder visibly aggregated when dissolved, which was still the case after optimization of the concentration and forced dispersion by sonification. Because of the resulting high variance in particle size both materials could not be measured properly by DLS. Furthermore, no results could be obtained for the strontium chloride powder: the amount of scattering was too low, even after significantly increasing the concentration of the dispersion. This can be explained by a hydrodynamic diameter below the detection limit of 10 nm. Silicate nano-powder had a mean hydrodynamic diameter of 67.49 nm (fig. 6). The hydrodynamic radius is by definition the radius of a sphere consisting of the actual particle, plus a layer of attracted solvent. After subtraction of this additional layer, which has an estimated thickness of 2-10 nm for particles dispersed in deionized water [117], an estimation of the actual diameter can be made. This validates the nano-size of the silicate nano-powder.

All the evaluated electrolyte suspensions showed a positive zeta potential of 30 mV or above at room temperature (table 5). Firstly, a suspension or colloid with a zeta potential with an absolute value of 30 mV or above is characterized by a good physical stability: the electrostatic repulsion between adjacent particles is strong enough to prevent (partial) agglomeration [118]. Charged particles can effectively migrate by electrophoresis under stable conditions, because the global electrostatic attraction of the anode/cathode exceeds local forces [72]. Secondly, the net positive charge, which is an attribute of chitosan's protonated amino groups, allows for cathodic EPD of the electrolyte. Addition of (nano-)materials to the electrolyte suspensions decreased the zeta potential, which can be explained by interactions with chitosan's protonated amino groups [80, 119, 120], resulting in a lower charge density.

EPD of pure chitosan (described in 1.7.1) and (nano-)composite coatings on the surface of the porous titanium was visualized by SEM imaging (fig.7 A-F). Assessment of the uniformity, thickness, and degradation of the coatings with optical techniques (SEM, FIB) was challenging. (Micro-) roughness and curvature of the ASM surface made it difficult to find an exact value for the coating thickness. The local chemical surface composition assessed by EDS (table 6), provided the elemental composition of the top layer of each sample. The ASM surface showed the presence of predominantly titanium and a small percentage of oxygen, which is related to the naturally occurring thin titanium oxide layer (TiO_2) with a thickness of approximately 1.5 to 10 nm under normal conditions [121]. The presence of chitosan can be found in the data of all coated samples in the form of elevated percentages of carbon, nitrogen, and oxygen [122]. The carbon to nitrogen ratio provided further proof for chitosan's presence. Ratios of approximately 10 can be observed in the data, which were close to the theoretical composition of (80% deacetylated) chitosan (6.4) [123]. The difference between the theoretical and observed ratio was explained in another study with similar findings: the ratio is probably increased by the presence of contamination of carbon [123]. The Si surface contained silicon and magnesium in a ratio of 2.5, which is

comparable with the ratio obtained from the chemical composition of the nano-silicate provided by the manufacturer (1.5) [124]. Lithium was most probably not detectable by EDS because its wt% in silicate nano powder is approximately 27 times smaller than that of silicon [124]. The presence of hydroxyapatite on the HA surface can be confirmed by the presence of both calcium and phosphorus, in a ratio (1.13) close to that of the theoretical composition of hydroxyapatite : $Ca_{10}(PO_4)_6(OH)_2$ [125]. The presence of strontium and chlorine, in a ratio of 0.35, can be observed at the Sr surface. The chemical composition of strontium chloride: $SrCl_2$, which has a similar ratio, supports that the deposition of the composite coating was successful. Finally, the increase of approximately 25 wt% of carbon at the GO surface, compared to the other coated surfaces, indicates that graphene oxide was successfully deposited.

The release profiles of Si, HA, and Sr (nano-)composite coatings showed a high burst release during the first day (fig. 9). Diffusion and hydrogel degradation are the main phenomena responsible for the release of ions out of the composite coating [63, 64]. Logically, this means that superficial layers of the composite coating release their load faster than the lower situated layers. This results in a high release of ions during the first period while the top layers deplete, followed by a lower gradual release when lower situated layers come in contact with the PBS. This burst release behavior of the loaded chitosan has been confirmed in several other studies [100, 126, 127]. The ratio of the total release of silicon ions to magnesium and lithium ions at day 14 is comparable to the theoretical value of the silicate nano-powder [124]. Unfortunately, the concentration of lithium ions could not be determined at each time point as its value dropped below the detection limit after day 1. The release profile of the Si sample confirmed the successful release of the degradation products of the silicate nano-powder. The release of calcium and phosphorus ions from the HA sample could also be observed in the release profile data. The great concentration difference between both ions is probably related to the presence of PBS as degradation medium, since PBS contains a high concentration of phosphorus [128]. Although burst release of phosphorus ions was clearly observable, small variances in the PBS concentration had a much greater effect on the measured concentration than the relatively low release from the samples. Because of this, the measured phosphorus ion release probably deviates from the actual release of phosphorus ions from the HA sample. Significant increased concentrations of strontium ions confirmed its effective release from the Sr samples. Finally, the low variance in ion release between the samples within the same group (n=3), validates that our EPD protocol, which is conducted in batches of one sample, can succeed in the production of consistent composite coatings.

Similar studies which realized composite coatings by EPD, can provide insight in the mechanism of co-deposition. Silicate and hydroxyapatite form net positively charged macromolecules by adsorption of the positively charged chitosan in the electrolyte suspension [79, 80, 113]. During electrophoretic deposition, these macromolecules coagulate around the cathode, after which the material gets entrapped during the solidification of chitosan (described in 1.7.1). The deposition mechanism of chitosan-graphene oxide is not fully investigated yet [129]. It is believed that graphene oxide can be co-deposited with hydrogels by entrapment in the hydrogel matrix during deposition, or that absorption of charged hydrogels on the GO surface leads to charged macromolecules which allow deposition by EPD [115]. EPD of chitosan-strontium is achieved via bonding of strontium ions to chitosan's amino or

hydroxyl groups [100]. The exact mechanisms of deposition, however, are also depending on the electrolyte suspension parameters like pH, and composition, which have a significant effect on the structural characteristics of the dissolved chitosan [130].

4.2 In Vitro assessment

This study showed signs of an inhibitory effect of chitosan on cell attachment and cell proliferation when compared to as manufactured porous titanium. An explanation for this behavior could be cell apoptosis due to the strong electrostatic interactions between the negatively charged components of the cell membrane and the cationic amino groups (NH_3^+) of chitosan [131]. In literature, however, the effect of chitosan on osteoblasts attachment, spreading, and growth, is debated [131]. The variance in outcomes is related to chitosan's material characteristics, which, because of the natural origin of this material, can vary significantly between different batches [132]. Furthermore, cells attached to coated surfaces could potentially loosen faster than those connected to the ASM surface because of degradation of the coating. This would lead to misleading in vitro results, since only attached cells were included in most experiments. The CSE results (fig. 21 A), validate a difference between ASM and CH samples, but cannot answer whether the measured difference in cell attachment solely arises from a higher cell morbidity, or that it is also influenced by other factors, such as: less optimal surface roughness, or electrostatic repulsion. Most probably a combination of cell morbidity and other factors is responsible for the reduced CSE. This follows from the well bottom DNA content (fig. 21 B), which showed that a greater number of cells were present at CH compared to ASM. This observation suggests that the difference in number of attached cells is at least partially resulting from non-cytotoxicity related factors, which result in less favorable binding to the coated surface.

Chitosan's antibacterial properties originate from its cationic amino groups (NH_3^+) [123]. Contact killing of bacteria is accomplished by binding of chitosan's cationic amino groups with the negatively charged components of the bacterial membrane. This bonding inhibits the growth of the bacteria and eventually leads to collapsing of the membrane, killing the bacteria [133, 134]. The antibacterial effect of chitosan could not be significantly verified in this study, although both the CFU value and SEM imaging seem to show a reduction in the number of attached bacteria. The small differences between ASM and CH could be explained by low thickness of the coating and local fluctuations. In that case, a percentage of the total surface will be protected against adherent bacteria but leave other regions exposed. SEM images of CH (fig. 27) demonstrate this effect: the dark region, which is covered by a thicker chitosan layer shows significantly less bacterial attachment and biofilm formation than the surrounding areas. No significant antibacterial effect against planktonic bacteria was observed, which is expected, since chitosan's antibacterial effect is dependent on direct contact with the bacterial membrane [133, 134].

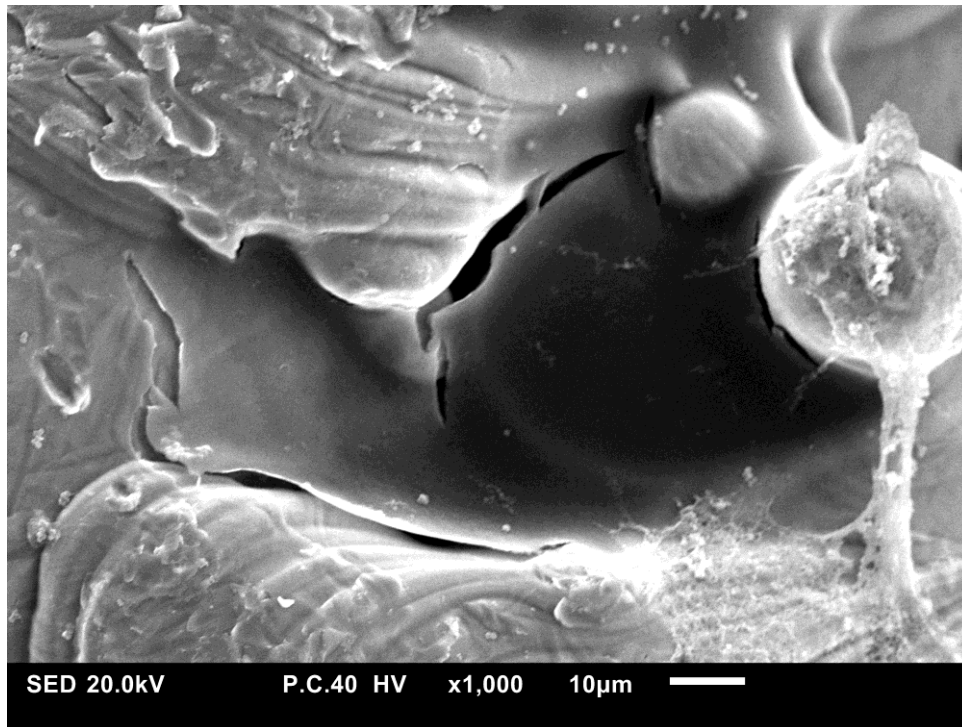


Figure 27: SEM image of chitosan's antibacterial effect

Since infection prevention and bone healing are both essential for orthopedic implants, (nano-)materials were incorporated in the chitosan coating in order to: improve the biocompatibility and osteogenic performance and (at least) maintain the intrinsic antibacterial properties. A selection process, based on alamar blue and live/dead assays, was performed to find the most promising concentrations for each of the materials. Analysis of the composite coated samples demonstrated that cytotoxic features are dose-dependent. This tendency is supported by other studies [82-84, 100, 135]. Unfortunately, empirically re-optimization of coating composition is often necessary, because potential antibacterial and cytotoxic effects are strongly dependent on the parameters of the production process, the source of materials, and the protocols used for assessment.

Si, HA, and Sr did not significantly improve the antibacterial properties of the porous titanium. Adherent *S. Aureus* seemed to be slightly inhibited by Si, HA, and Sr (± 0.5 log) compared to ASM (fig. 19). This effect is probably solely caused by the presence of chitosan. This is confirmed by the absence of an antibacterial effect of Si, HA, and Sr on planktonic bacteria (fig. 20), which means that the ion release did not result in significant inhibition. Other similar studies found that hydroxyapatite's good affinity to cell surface proteins and lipids does not only favor cells but bacteria as well, concluding that antibacterial effects arise from chitosan's presence [136, 137]. The local increased number of bacteria and biofilm formation at the surface of HA observed by SEM (fig. 18) could result from this characteristic of hydroxyapatite. Nano-silicate and strontium ions have not (yet) been linked to improved antibacterial efficiency [138]. The local increase of biofilm formation observed for Si could arise from an increase in non-selective binding sites on the chitosan coating by presence of nano-silicate, following the same mechanism as hydroxyapatite.

The CSE results (fig. 21) indicated that HA and Si, and to a less extent, GO and Sr, can improve the initial attachment of cells. Previous studies (summarized in 1.7.2) report similar findings: HA, Si, and GO, have an increased number of cell binding sites and nano-roughness compared to CH. The Alamar blue assay was conducted on both attached cells and a seeded monolayer to elucidate the source of cytotoxicity. The metabolic activity of attached cells (fig. 22, 23) gave an indication of the effect of direct cell contact with the coating. The metabolic activity of the monolayer, on the other hand, gave an indication of the effect of the release of ions and degradation products. Comparison of both results confirms that chitosan's cytotoxicity is mainly originating from direct cell contact. The (burst) release of ions, and the altered surface composition, did seem to slightly improve the cytocompatibility of the coated samples compared to CH, although a significant effect of the composite coatings of Si, HA, and Sr, on viability of attached cells was not observable. The viability and proliferation of the monolayer is in line with this observation, no significant improvements are realized by Si, HA, and Sr. GO seemed to improve the viability of attached cells at the later time points, and significantly improved the viability of the monolayer reaching a absorbance six times higher than ASM at day 7. The positive (dose dependent) effect of GO was also observed in other studies [107, 135]. This effect can be attributed to increased surface area, improved wettability, and improved surface roughness [139, 140].

The ALP activity of attached cells was not significantly different among the groups (fig. 24). The difference between ASM and the coated samples is in line with the Alamar blue assay. The results can be explained by an early cytotoxicity of the chitosan coating followed by gradual recovery after the first days. The immunostaining at day 1 (fig.25) could not provide information on the cell morphology due to overlapping cells, and surface irregularities, which made it impossible to successfully focus the microscope on larger areas. The DAPI-staining of the cell nuclei showed that CH contained an increased number of cells. This does not follow the trend of this study and is probably caused by the staining of dead cells which are still attached to the surface by electrostatic interactions. The amount and quality of the extracted RNA was too low at day 1 and day 11 to provide information on osteogenic differentiation (table 7). No significant up-regulation of osteogenic markers was observed at day 21. High variance of expression levels within groups suggests that the local conditions on the surface of the samples are non-homogeneous. The reported effects of the (nano-)materials incorporated in the chitosan coating of Si, HA, and Sr (summarized in 1.7.2), on both cytocompatibility and osteogenic performance, could not be confirmed in this study.

4.3 Limitations & future research

The particle size distribution could not be evaluated for all materials using DLS. This meant that the results could not all be related to the specific particle size. Transmission electron microscopy (TEM), small angle X-ray scattering (SAXS), or acoustic resonance spectroscopy (ARS), could be used to further investigate particle size in future research.

The curvature, roughness, and porosity of the porous structure limited the evaluation of the EPD process: the coating thickness, uniformity and degradation behavior could not be optimally analyzed by SEM, EDS, and FIB. Future research could further analyze the coating characteristics by creating cross-sections for inspection of the inner struts. The Live/dead assay and immunostaining could also benefit from creating cross-sections, allowing inspection of attached cells near the center of the scaffold.

The number of samples for the in vitro assessment was too low to statistically confirm most of the observed trends and effects. Future studies should increase the number of samples per group to improve the statistical power of the experiments. GO showed promising results in terms of cell viability and proliferation and should be further examined on antibacterial efficiency and osteogenic performance in future experiments. Hydrogel modifications and re-optimization of the EPD process could be performed to change the burst release behavior of the (nano-)composite coatings and find the optimal release pattern. Furthermore, combinations of the inorganic (nano-)materials used in this study could be applied to search for possible synergistic effects.

A great limitation of the in vitro tests performed in this study is their static nature. Dynamic flow systems could improve the simulation of physiological conditions. In vivo experiments can be conducted to further analyze the effects of novel coating concepts under physiological conditions.

Finally, future research could benefit from (further) standardized coating protocols and input materials. Minor changes in protocol and material can result in great differences in outcomes, because in vitro assessment is quite delicate. Standardized tests and protocols can improve the comparability between different studies and potentially speed up the development of the next generation of functional coatings.

5. Conclusion

This study showed the successful electrophoretic deposition of (nano-)composite coatings on direct metal printed porous titanium. Chitosan, functioning as a hydrogel carrier, was co-deposited with respectively silicate nano-powder, hydroxyapatite nano-powder, strontium chloride powder, and graphene oxide. Evidence of surface morphology, chemical composition, and release profile verified the deposition of the different (nano-) composite coatings. A slight antibacterial effect of coated samples, related to the presence of chitosan, was observed against adherent *S. Aureus*, which was not improved by the presence of the additional components of the (nano-)composite coatings. Chitosan's cytotoxic features mainly apply to direct attached cells. Only the graphene oxide composite coatings showed a significant improvement of cytocompatibility. No significant improvement of the osteogenic performance of porous titanium was achieved by the (composite) coating process. Conclusively, the (nano-)composite coatings which were evaluated in this study, could not substantially improve the in vitro performance of porous titanium.

References

1. Co, H.W., *Orthopedic industry overview*. 2014.
2. Gavrilov, L.A. and P. Heuveline, *Aging of population*. The encyclopedia of population, 2003. **1**: p. 32-37.
3. Moran, C. and T. Horton, *Total knee replacement: the joint of the decade*. 2000, British Medical Journal Publishing Group.
4. Danoff, J.R., et al., *Total knee arthroplasty considerations in rheumatoid arthritis*. Autoimmune diseases, 2013. **2013**.
5. Ravi, B., et al., *A systematic review and meta-analysis comparing complications following total joint arthroplasty for rheumatoid arthritis versus for osteoarthritis*. Arthritis & Rheumatology, 2012. **64**(12): p. 3839-3849.
6. Cypher, T.J. and J.P. Grossman, *Biological principles of bone graft healing*. The Journal of foot and ankle surgery, 1996. **35**(5): p. 413-417.
7. Phelps, E.A., et al., *Bioartificial matrices for therapeutic vascularization*. Proceedings of the National Academy of Sciences, 2010. **107**(8): p. 3323-3328.
8. Wu, S., et al., *Biomimetic porous scaffolds for bone tissue engineering*. Materials Science and Engineering: R: Reports, 2014. **80**: p. 1-36.
9. Hamed, E., et al., *Multi-scale modelling of elastic moduli of trabecular bone*. Journal of The Royal Society Interface, 2012: p. rsif20110814.
10. Hamed, E., et al., *Elastic moduli of untreated, demineralized and deproteinized cortical bone: validation of a theoretical model of bone as an interpenetrating composite material*. Acta biomaterialia, 2012. **8**(3): p. 1080-1092.
11. Dimitriou, R., E. Tsiridis, and P.V. Giannoudis, *Current concepts of molecular aspects of bone healing*. Injury, 2005. **36**(12): p. 1392-1404.
12. Marsell, R. and T.A. Einhorn, *The biology of fracture healing*. Injury, 2011. **42**(6): p. 551-5.
13. Mehta, M., et al., *Biomaterial delivery of morphogens to mimic the natural healing cascade in bone*. Adv Drug Deliv Rev, 2012. **64**(12): p. 1257-76.
14. Novosel, E.C., C. Kleinhans, and P.J. Kluger, *Vascularization is the key challenge in tissue engineering*. Adv Drug Deliv Rev, 2011. **63**(4-5): p. 300-11.
15. Claes, L.E., et al., *Effects of mechanical factors on the fracture healing process*. Clinical orthopaedics and related research, 1998. **355**: p. S132-S147.
16. Huiskes, R., H. Weinans, and B. Van Rietbergen, *The relationship between stress shielding and bone resorption around total hip stems and the effects of flexible materials*. Clinical orthopaedics and related research, 1992. **274**: p. 124-134.
17. Widmer, A.F., *New developments in diagnosis and treatment of infection in orthopedic implants*. 2001, Oxford University Press.
18. Zimmermann, G. and A. Moghaddam, *Allograft bone matrix versus synthetic bone graft substitutes*. Injury, 2011. **42**: p. S16-S21.
19. Nouri, A., P.D. Hodgson, and C.e. Wen, *Biomimetic porous titanium scaffolds for orthopaedic and dental applications*. 2010: InTech.
20. Manivasagam, G., D. Dhinasekaran, and A. Rajamanickam, *Biomedical implants: Corrosion and its prevention-a review*. Recent patents on corrosion science, 2010. **2**(1): p. 40-54.
21. Anderson, J.M. and J.J. Langone, *Issues and perspectives on the biocompatibility and immunotoxicity evaluation of implanted controlled release systems*. Journal of controlled release, 1999. **57**(2): p. 107-113.
22. Geetha, M., et al., *Ti based biomaterials, the ultimate choice for orthopaedic implants—a review*. Progress in materials science, 2009. **54**(3): p. 397-425.

23. Rack, H. and J. Qazi, *Titanium alloys for biomedical applications*. Materials Science and Engineering: C, 2006. **26**(8): p. 1269-1277.
24. Sing, S.L., et al., *Laser and electron-beam powder-bed additive manufacturing of metallic implants: A review on processes, materials and designs*. Journal of Orthopaedic Research, 2016. **34**(3): p. 369-385.
25. Frazier, W.E., *Metal additive manufacturing: a review*. Journal of Materials Engineering and Performance, 2014. **23**(6): p. 1917-1928.
26. Taniguchi, N., et al., *Effect of pore size on bone ingrowth into porous titanium implants fabricated by additive manufacturing: An in vivo experiment*. Mater Sci Eng C Mater Biol Appl, 2016. **59**: p. 690-701.
27. Wang, X., et al., *Topological design and additive manufacturing of porous metals for bone scaffolds and orthopaedic implants: A review*. Biomaterials, 2016. **83**: p. 127-41.
28. Zadpoor, A.A. and J. Malda, *Additive Manufacturing of Biomaterials, Tissues, and Organs*. 2017, Springer.
29. Aly, M.S., W. Bleck, and P.-F. Scholz, *How metal foams behave if the temperature rises*. Metal Powder Report, 2005. **60**(10): p. 38-45.
30. Karageorgiou, V. and D. Kaplan, *Porosity of 3D biomaterial scaffolds and osteogenesis*. Biomaterials, 2005. **26**(27): p. 5474-91.
31. Sumner, D.R., et al., *Experimental studies of bone remodeling in total hip arthroplasty*. Clinical orthopaedics and related research, 1992. **276**: p. 83-90.
32. Kuboki, Y., et al., *BMP-induced osteogenesis on the surface of hydroxyapatite with geometrically feasible and nonfeasible structures: topology of osteogenesis*. Journal of biomedical materials research, 1998. **39**(2): p. 190-199.
33. van der Stok, J., et al., *Enhanced bone regeneration of cortical segmental bone defects using porous titanium scaffolds incorporated with colloidal gelatin gels for time- and dose-controlled delivery of dual growth factors*. Tissue Eng Part A, 2013. **19**(23-24): p. 2605-14.
34. Amin Yavari, S., et al., *Bone regeneration performance of surface-treated porous titanium*. Biomaterials, 2014. **35**(24): p. 6172-81.
35. Yin, B., et al., *Hybrid Macro-Porous Titanium Ornamented by Degradable 3D Gel/nHA Micro-Scaffolds for Bone Tissue Regeneration*. Int J Mol Sci, 2016. **17**(4).
36. Jiang, T., et al., *Functionalization of chitosan/poly (lactic acid-glycolic acid) sintered microsphere scaffolds via surface heparinization for bone tissue engineering*. Journal of Biomedical Materials Research Part A, 2010. **93**(3): p. 1193-1208.
37. Nune, K.C., et al., *Osteoblast functions in functionally graded Ti-6Al-4 V mesh structures*. J Biomater Appl, 2016. **30**(8): p. 1182-204.
38. Liu, X., P. Chu, and C. Ding, *Surface modification of titanium, titanium alloys, and related materials for biomedical applications*. Materials Science and Engineering: R: Reports, 2004. **47**(3-4): p. 49-121.
39. Zhao, L., et al., *The influence of hierarchical hybrid micro/nano-textured titanium surface with titania nanotubes on osteoblast functions*. Biomaterials, 2010. **31**(19): p. 5072-82.
40. Sul, Y.-T., et al., *Characteristics of the surface oxides on turned and electrochemically oxidized pure titanium implants up to dielectric breakdown:: the oxide thickness, micropore configurations, surface roughness, crystal structure and chemical composition*. Biomaterials, 2002. **23**(2): p. 491-501.
41. Jiang, P., J. Liang, and C. Lin, *Construction of micro-nano network structure on titanium surface for improving bioactivity*. Applied Surface Science, 2013. **280**: p. 373-380.
42. Bjursten, L.M., et al., *Titanium dioxide nanotubes enhance bone bonding in vivo*. Journal of Biomedical Materials Research Part A, 2010. **92**(3): p. 1218-1224.

43. Brammer, K.S., et al., *Improved bone-forming functionality on diameter-controlled TiO₂ nanotube surface*. *Acta biomaterialia*, 2009. **5**(8): p. 3215-3223.
44. Liu, X., P.K. Chu, and C. Ding, *Surface modification of titanium, titanium alloys, and related materials for biomedical applications*. *Materials Science and Engineering: R: Reports*, 2004. **47**(3): p. 49-121.
45. Ulijn, R.V., et al., *Bioresponsive hydrogels*. *Materials Today*, 2007. **10**(4): p. 40-48.
46. Kim, T.G., H. Shin, and D.W. Lim, *Biomimetic Scaffolds for Tissue Engineering*. *Advanced Functional Materials*, 2012. **22**(12): p. 2446-2468.
47. Slaughter, B.V., et al., *Hydrogels in regenerative medicine*. *Adv Mater*, 2009. **21**(32-33): p. 3307-29.
48. Annabi, N., et al., *25th Anniversary Article: Rational Design and Applications of Hydrogels in Regenerative Medicine*. *Advanced Materials*, 2014. **26**(1): p. 85-124.
49. Ahadian, S., et al., *Bioconjugated Hydrogels for Tissue Engineering and Regenerative Medicine*. *Bioconjug Chem*, 2015. **26**(10): p. 1984-2001.
50. Lee, S.C., I.K. Kwon, and K. Park, *Hydrogels for delivery of bioactive agents: a historical perspective*. *Adv Drug Deliv Rev*, 2013. **65**(1): p. 17-20.
51. Drury, J.L. and D.J. Mooney, *Hydrogels for tissue engineering: scaffold design variables and applications*. *Biomaterials*, 2003. **24**(24): p. 4337-4351.
52. Chen, R.R. and D.J. Mooney, *Polymeric growth factor delivery strategies for tissue engineering*. *Pharmaceutical research*, 2003. **20**(8): p. 1103-1112.
53. Yang, Q., et al., *Composites of functional polymeric hydrogels and porous membranes*. *J. Mater. Chem.*, 2011. **21**(9): p. 2783-2811.
54. Ingber, D.E., *Cellular mechanotransduction: putting all the pieces together again*. *The FASEB journal*, 2006. **20**(7): p. 811-827.
55. Wang, B., et al., *The shear strength and the failure mode of plasma-sprayed hydroxyapatite coating to bone: The effect of coating thickness*. *Journal of Biomedical Materials Research Part A*, 1993. **27**(10): p. 1315-1327.
56. Gaharwar, A.K., N.A. Peppas, and A. Khademhosseini, *Nanocomposite hydrogels for biomedical applications*. *Biotechnol Bioeng*, 2014. **111**(3): p. 441-53.
57. von der Mark, K., et al., *Nanoscale engineering of biomimetic surfaces: cues from the extracellular matrix*. *Cell Tissue Res*, 2010. **339**(1): p. 131-53.
58. Utech, S. and A.R. Boccaccini, *A review of hydrogel-based composites for biomedical applications: enhancement of hydrogel properties by addition of rigid inorganic fillers*. *Journal of materials science*, 2016. **51**(1): p. 271-310.
59. Kim, J., et al., *Bone regeneration using hyaluronic acid-based hydrogel with bone morphogenic protein-2 and human mesenchymal stem cells*. *Biomaterials*, 2007. **28**(10): p. 1830-7.
60. Park, K.H., et al., *Bone morphogenic protein-2 (BMP-2) loaded nanoparticles mixed with human mesenchymal stem cell in fibrin hydrogel for bone tissue engineering*. *J Biosci Bioeng*, 2009. **108**(6): p. 530-7.
61. Hoare, T.R. and D.S. Kohane, *Hydrogels in drug delivery: progress and challenges*. *Polymer*, 2008. **49**(8): p. 1993-2007.
62. Gupta, R., Q. Beg, and P. Lorenz, *Bacterial alkaline proteases: molecular approaches and industrial applications*. *Applied microbiology and biotechnology*, 2002. **59**(1): p. 15-32.
63. Amsden, B., *Solute diffusion within hydrogels. Mechanisms and models*. *Macromolecules*, 1998. **31**(23): p. 8382-8395.
64. Langer, R. and N.A. Peppas, *Advances in biomaterials, drug delivery, and bionanotechnology*. *AIChE Journal*, 2003. **49**(12): p. 2990-3006.

65. Boccaccini, A., et al., *Electrophoretic deposition of biomaterials*. Journal of the Royal Society Interface, 2010. **7**(Suppl 5): p. S581-S613.
66. Kerativitayanan, P., J.K. Carrow, and A.K. Gaharwar, *Nanomaterials for Engineering Stem Cell Responses*. Adv Healthc Mater, 2015. **4**(11): p. 1600-27.
67. Costa, R.R. and J.F. Mano, *Polyelectrolyte multilayered assemblies in biomedical technologies*. Chem Soc Rev, 2014. **43**(10): p. 3453-79.
68. Seon, L., et al., *Polyelectrolyte Multilayers: A Versatile Tool for Preparing Antimicrobial Coatings*. Langmuir, 2015. **31**(47): p. 12856-72.
69. Hassert, R. and A.G. Beck-Sickinger, *Tuning peptide affinity for biofunctionalized surfaces*. Eur J Pharm Biopharm, 2013. **85**(1): p. 69-77.
70. Yuk, H., et al., *Tough bonding of hydrogels to diverse non-porous surfaces*. Nat Mater, 2016. **15**(2): p. 190-6.
71. Van der Biest, O.O. and L.J. Vandeperre, *Electrophoretic deposition of materials*. Annual Review of Materials Science, 1999. **29**(1): p. 327-352.
72. Besra, L. and M. Liu, *A review on fundamentals and applications of electrophoretic deposition (EPD)*. Progress in Materials Science, 2007. **52**(1): p. 1-61.
73. Sarkar, P. and P.S. Nicholson, *Electrophoretic deposition (EPD): mechanisms, kinetics, and application to ceramics*. Journal of the American Ceramic Society, 1996. **79**(8): p. 1987-2002.
74. Muzzarelli, R.A., *Chitins and chitosans for the repair of wounded skin, nerve, cartilage and bone*. Carbohydrate polymers, 2009. **76**(2): p. 167-182.
75. Berger, J., et al., *Structure and interactions in covalently and ionically crosslinked chitosan hydrogels for biomedical applications*. European Journal of Pharmaceutics and Biopharmaceutics, 2004. **57**(1): p. 19-34.
76. Liu, H., et al., *Chitosan kills bacteria through cell membrane damage*. International journal of food microbiology, 2004. **95**(2): p. 147-155.
77. Berger, J., R. Gurny, and M.R. Oechsli, *Pseudo-thermosetting neutralized chitosan composition forming a hydrogel and a process for producing the same*. 2014, Google Patents.
78. Sun, F., X. Pang, and I. Zhitomirsky, *Electrophoretic deposition of composite hydroxyapatite–chitosan–heparin coatings*. Journal of Materials Processing Technology, 2009. **209**(3): p. 1597-1606.
79. Pang, X. and I. Zhitomirsky, *Electrophoretic deposition of composite hydroxyapatite-chitosan coatings*. Materials Characterization, 2007. **58**(4): p. 339-348.
80. Grandfield, K. and I. Zhitomirsky, *Electrophoretic deposition of composite hydroxyapatite–silica–chitosan coatings*. Materials Characterization, 2008. **59**(1): p. 61-67.
81. Hoppe, A., N.S. Güldal, and A.R. Boccaccini, *A review of the biological response to ionic dissolution products from bioactive glasses and glass-ceramics*. Biomaterials, 2011. **32**(11): p. 2757-2774.
82. Zhang, W., et al., *Effects of strontium in modified biomaterials*. Acta Biomater, 2011. **7**(2): p. 800-8.
83. Dawson, J.I. and R.O. Oreffo, *Clay: new opportunities for tissue regeneration and biomaterial design*. Adv Mater, 2013. **25**(30): p. 4069-86.
84. Gaharwar, A.K., et al., *Bioactive silicate nanoplatelets for osteogenic differentiation of human mesenchymal stem cells*. Adv Mater, 2013. **25**(24): p. 3329-36.
85. Lee, J.H., et al., *Control of Osteogenic Differentiation and Mineralization of Human Mesenchymal Stem Cells on Composite Nanofibers Containing Poly [lactic-co-(glycolic acid)] and Hydroxyapatite*. Macromolecular bioscience, 2010. **10**(2): p. 173-182.
86. Xue, D., et al., *Osteochondral repair using porous poly (lactide-co-glycolide)/nano-hydroxyapatite hybrid scaffolds with undifferentiated mesenchymal*

- stem cells in a rat model*. Journal of Biomedical Materials Research Part A, 2010. **94**(1): p. 259-270.
87. Marie, P.J., *The calcium-sensing receptor in bone cells: a potential therapeutic target in osteoporosis*. Bone, 2010. **46**(3): p. 571-576.
 88. Julien, M., et al., *Phosphate-Dependent Regulation of MGP in Osteoblasts: Role of ERK1/2 and Fra-1*. Journal of Bone and Mineral Research, 2009. **24**(11): p. 1856-1868.
 89. Seyedjafari, E., et al., *Nanohydroxyapatite-coated electrospun poly (l-lactide) nanofibers enhance osteogenic differentiation of stem cells and induce ectopic bone formation*. Biomacromolecules, 2010. **11**(11): p. 3118-3125.
 90. Chang, C.-W., et al., *PEG/clay nanocomposite hydrogel: a mechanically robust tissue engineering scaffold*. Soft Matter, 2010. **6**(20): p. 5157-5164.
 91. Carlisle, E.M., *Silicon: a requirement in bone formation independent of vitamin D 1*. Calcified tissue international, 1981. **33**(1): p. 27-34.
 92. Zreiqat, H., et al., *Mechanisms of magnesium-stimulated adhesion of osteoblastic cells to commonly used orthopaedic implants*. Journal of biomedical materials research, 2002. **62**(2): p. 175-184.
 93. Rude, R.K., et al., *Dietary magnesium reduction to 25% of nutrient requirement disrupts bone and mineral metabolism in the rat*. Bone, 2005. **37**(2): p. 211-219.
 94. Reffitt, D., et al., *Orthosilicic acid stimulates collagen type 1 synthesis and osteoblastic differentiation in human osteoblast-like cells in vitro*. Bone, 2003. **32**(2): p. 127-135.
 95. Boivin, G., et al., *Strontium distribution and interactions with bone mineral in monkey iliac bone after strontium salt (S 12911) administration*. Journal of Bone and Mineral Research, 1996. **11**(9): p. 1302-1311.
 96. Nielsen, S.P., *The biological role of strontium*. Bone, 2004. **35**(3): p. 583-588.
 97. Park, J.W., et al., *Osteoblast response and osseointegration of a Ti-6Al-4V alloy implant incorporating strontium*. Acta Biomater, 2010. **6**(7): p. 2843-51.
 98. Andersen, O.Z., et al., *Accelerated bone ingrowth by local delivery of strontium from surface functionalized titanium implants*. Biomaterials, 2013. **34**(24): p. 5883-90.
 99. Chung, C.J. and H.Y. Long, *Systematic strontium substitution in hydroxyapatite coatings on titanium via micro-arc treatment and their osteoblast/osteoclast responses*. Acta Biomater, 2011. **7**(11): p. 4081-7.
 100. Ma, K., et al., *Surface functionalization with strontium-containing nanocomposite coatings via EPD*. Colloids Surf B Biointerfaces, 2016. **146**: p. 97-106.
 101. Nardone, V., et al., *Osteodifferentiation of human preadipocytes induced by strontium released from hydrogels*. Int J Biomater, 2012. **2012**: p. 865291.
 102. Hurtel-Lemaire, A.S., et al., *The calcium-sensing receptor is involved in strontium ranelate-induced osteoclast apoptosis new insights into the associated signaling pathways*. Journal of Biological Chemistry, 2009. **284**(1): p. 575-584.
 103. Nayak, T.R., et al., *Graphene for controlled and accelerated osteogenic differentiation of human mesenchymal stem cells*. arXiv preprint arXiv:1104.5120, 2011.
 104. Lee, W.C., et al., *Origin of enhanced stem cell growth and differentiation on graphene and graphene oxide*. ACS nano, 2011. **5**(9): p. 7334-7341.
 105. Chen, G.-Y., et al., *A graphene-based platform for induced pluripotent stem cells culture and differentiation*. Biomaterials, 2012. **33**(2): p. 418-427.
 106. Tatavarty, R., et al., *Synergistic acceleration in the osteogenesis of human mesenchymal stem cells by graphene oxide-calcium phosphate nanocomposites*. Chemical Communications, 2014. **50**(62): p. 8484-8487.

107. Ordikhani, F., et al., *Physicochemical and biological properties of electrodeposited graphene oxide/chitosan films with drug-eluting capacity*. Carbon, 2015. **84**: p. 91-102.
108. Gu, M., et al., *Is graphene a promising nano-material for promoting surface modification of implants or scaffold materials in bone tissue engineering?* Tissue Engineering Part B: Reviews, 2014. **20**(5): p. 477-491.
109. Krall, E.A. and B. Dawson-Hughes, *Heritable and life-style determinants of bone mineral density*. Journal of Bone and Mineral Research, 1993. **8**(1): p. 1-9.
110. Leng, H., et al., *Effect of age on mechanical properties of the collagen phase in different orientations of human cortical bone*. Bone, 2013. **55**(2): p. 288-291.
111. Liu, G., et al., *Quinone-mediated microbial synthesis of reduced graphene oxide with peroxidase-like activity*. Bioresource technology, 2013. **149**: p. 503-508.
112. Wang, G., et al., *Microbial reduction of graphene oxide by Shewanella*. Nano Research, 2011. **4**(6): p. 563-570.
113. Pang, X. and I. Zhitomirsky, *Electrodeposition of composite hydroxyapatite–chitosan films*. Materials Chemistry and Physics, 2005. **94**(2-3): p. 245-251.
114. Ordikhani, F., M. Dehghani, and A. Simchi, *Antibiotic-loaded chitosan–Laponite films for local drug delivery by titanium implants: cell proliferation and drug release studies*. Journal of Materials Science: Materials in Medicine, 2015. **26**(12): p. 269.
115. Li, M., et al., *Electrophoretic deposition and electrochemical behavior of novel graphene oxide-hyaluronic acid-hydroxyapatite nanocomposite coatings*. Applied Surface Science, 2013. **284**: p. 804-810.
116. Kodama, H.-a., et al., *Establishment of a clonal osteogenic cell line from newborn mouse calvaria*. 歯科基礎医学会雑誌, 1981. **23**(4): p. 899-901.
117. Bhattacharjee, S., *DLS and zeta potential - What they are and what they are not?* J Control Release, 2016. **235**: p. 337-51.
118. Radomska-Soukharev, A., *Stability of lipid excipients in solid lipid nanoparticles*. Advanced drug delivery reviews, 2007. **59**(6): p. 411-418.
119. Rhazi, M., et al., *Influence of the nature of the metal ions on the complexation with chitosan.: Application to the treatment of liquid waste*. European Polymer Journal, 2002. **38**(8): p. 1523-1530.
120. Grandfield, K., et al., *Electrophoretic deposition of polymer-carbon nanotube–hydroxyapatite composites*. Surface and Coatings Technology, 2009. **203**(10-11): p. 1481-1487.
121. Kuromoto, N.K., R.A. Simão, and G.A. Soares, *Titanium oxide films produced on commercially pure titanium by anodic oxidation with different voltages*. Materials Characterization, 2007. **58**(2): p. 114-121.
122. Rinaudo, M., *Chitin and chitosan: properties and applications*. Progress in polymer science, 2006. **31**(7): p. 603-632.
123. Desai, K., et al., *Nanofibrous chitosan non-wovens for filtration applications*. Polymer, 2009. **50**(15): p. 3661-3669.
124. instruments, B.A., *Technical information, Laponite, Performance Additives*.
125. LeGeros, R.Z., *Properties of osteoconductive biomaterials: calcium phosphates*. Clinical orthopaedics and related research, 2002. **395**: p. 81-98.
126. Place, E.S., et al., *Strontium- and zinc-alginate hydrogels for bone tissue engineering*. Tissue Eng Part A, 2011. **17**(21-22): p. 2713-22.
127. Sinha, V.R., et al., *Chitosan microspheres as a potential carrier for drugs*. Int J Pharm, 2004. **274**(1-2): p. 1-33.

128. Morrison, M., et al., *The electrochemical evaluation of a Zr-based bulk metallic glass in a phosphate-buffered saline electrolyte*. Journal of Biomedical Materials Research Part A, 2005. **74**(3): p. 430-438.
129. Diba, M., et al., *Electrophoretic deposition of graphene-related materials: A review of the fundamentals*. Progress in Materials Science, 2016. **82**: p. 83-117.
130. Guibal, E., *Interactions of metal ions with chitosan-based sorbents: a review*. Separation and Purification Technology, 2004. **38**(1): p. 43-74.
131. Jiang, T., et al., *Surface functionalization of titanium with chitosan/gelatin via electrophoretic deposition: characterization and cell behavior*. Biomacromolecules, 2010. **11**(5): p. 1254-1260.
132. Hamilton, V., et al., *Bone cell attachment and growth on well-characterized chitosan films*. Polymer International, 2007. **56**(5): p. 641-647.
133. Raafat, D. and H.G. Sahl, *Chitosan and its antimicrobial potential—a critical literature survey*. Microbial biotechnology, 2009. **2**(2): p. 186-201.
134. Rabea, E.I., et al., *Chitosan as antimicrobial agent: applications and mode of action*. Biomacromolecules, 2003. **4**(6): p. 1457-1465.
135. Mahmoudi, N. and A. Simchi, *On the biological performance of graphene oxide-modified chitosan/polyvinyl pyrrolidone nanocomposite membranes: In vitro and in vivo effects of graphene oxide*. Mater Sci Eng C Mater Biol Appl, 2017. **70**(Pt 1): p. 121-131.
136. Shi, Y., et al., *Electrophoretic deposition of graphene oxide reinforced chitosan–hydroxyapatite nanocomposite coatings on Ti substrate*. Journal of Materials Science: Materials in Medicine, 2016. **27**(3): p. 48.
137. Liu, Y., et al., *Deposition, characterization, and enhanced adherence of Escherichia coli bacteria on flame-sprayed photocatalytic titania-hydroxyapatite coatings*. Journal of thermal spray technology, 2013. **22**(6): p. 1053-1062.
138. Dabsie, F., et al., *Does strontium play a role in the cariostatic activity of glass ionomer?: Strontium diffusion and antibacterial activity*. journal of dentistry, 2009. **37**(7): p. 554-559.
139. Talukdar, Y., et al., *The effects of graphene nanostructures on mesenchymal stem cells*. Biomaterials, 2014. **35**(18): p. 4863-4877.
140. Kim, J., et al., *Graphene-incorporated chitosan substrata for adhesion and differentiation of human mesenchymal stem cells*. Journal of Materials Chemistry B, 2013. **1**(7): p. 933-938.